High-Speed Indoor MIMO Visible Light Communications



Fangxiao Dong

Mansfield College

University of Oxford

Supervisor: Professor Dominic O'Brien

A thesis submitted for the degree of

Master by Research in Engineering Science

Trinity 2021

ABSTRACT

Mobile data traffic has experienced exponential growth in recent decades, which imposes increasing pressure on the limited resources of wireless communications. Meanwhile, the increased use of white light-emitting diodes (LEDs) has led to a growing interest in a novel wireless communications technology: Indoor visible light communication (VLC). The unlicensed spectrum provided by VLC supplies the additional capacity to mobile communication systems, while the LEDs can also offer illumination. This illumination is often provided by multiple LEDs installed on the ceiling in an indoor environment, which offers the potential to develop Multiple-Input Multiple-Output (MIMO) VLC systems. MIMO systems are subject to crosstalk between the multiple communications channels and mitigating this crosstalk is an active area of research. This thesis focuses on how to best use the MIMO resource regarding the complexity of implementation and control of such a system.

First, the work focuses on a high-speed indoor MIMO-VLC system that optimises the number of MIMO channels and the data rates. A Channel Condition-based Transmitter Coordination (CCTC) algorithm is proposed. In the CCTC algorithm, transmitters are coordinated to form one or several group(s) based on the wireless channel conditions, then the data rate of each group is optimised separately. The system employs zero-forcing MIMO equalisation and decision-feedback equalisation (DFE) to mitigate crosstalk. Two receiver designs have also been employed: A seven-channel angle diversity receiver (ADR) and an aperture-based receiver (ABR). In the new system, the overall data rates are on average 41 per cent (with an ADR) and 127 per cent (with an ABR) higher than that in the conventional spatial multiplexing approach. Moreover, the peak overall data rate of the system with an ADR (676 Mbps) is 56 per cent higher than that with an ABR (434 Mbps), which means that an ADR shows better performance than an ABR when they are in a similar size. The proposed approach

efficiently mitigates the crosstalk and improves the data rates in the MIMO system. However, it employs exhaustive search to coordinate transmitters and data rates, which takes a large amount of computing time.

A solution with less computational complexity is therefore explored. A neural network is employed to replace the proposed algorithm to obtain optimal results. The neural network is trained and tested with varying receiver positions, yaw rotation angles, or roll rotation angles relative to the lighting sources. A statistical model with random orientations and receiver positions depicting a user walking in the coverage area is also employed. The results show that the neural network-based system saves a factor of three to four in computing time compared with the CCTC algorithm system while achieving the same level of performance. The water-filling algorithm is employed as a benchmark of the maximum capacity of the system to assess the neural network performance. The neural network only takes one-third of the computing time compared to the water-filling algorithm, with a 12 per cent data rate penalty on average. Moreover, it is simpler in terms of control and implementation than the water-filling algorithm. These results show the potential of the more straightforward neural network method, and future directions for this work are presented in the conclusions of the thesis.

ACKNOWLEDGEMENTS

I would like to express my deepest gratitude to my supervisor Professor Dominic O'Brien for his supervision, as well as his continuous support, invaluable inspiration, and utmost patience during my two years' research.

I would also appreciate members in the Communication Research Group, especially Dr Ravinder Singh, Paramin PM Sangwongngam, Vincent Lee, Jiaruo Yan, Amna Riaz, Dr Wajahat Ali and Zijing Wang, for the valuable discussions and creative ideas.

I owe my sincere gratitude to my parents for their unconditional love and enduring support. Especially, I would like to thank my fiancé, Bohan Jiang, for his selfless love and encouragement during my research journey.

PUBLICATIONS

[1] F. Dong, and D. O'Brien, 'High Speed Adaptive MIMO-VLC System with Neural Network' (submitted to the *Journal of Lightwave Technology*).

[2] F. Dong, and D. O'Brien, 'A Neural Network-based Adaptive MIMO-VLC System', in *2021 IEEE Photonics Conference (IPC)*, Oct. 2021.

[3] F. Dong, R. Singh, and D. O'Brien, 'Adaptive MIMO-VLC System for High Data Rate Communications', in *2020 IEEE Globecom Workshops (GC Wkshps)*, Taipei, Taiwan, Dec. 2020.

TABLE OF CONTENTS

Abstract **1**

Acknowledgements **3**

Publications **4**

Table of Contents **5**

List of Figures **7**

List of Tables **10**

List of Acronyms **11**

Chapter I: Introduction **13**

1.1. Demand for Wireless Communications 13

1.2. Visible Light Communications 14

1.3. MIMO-VLC System 19

1.4. MIMO-VLC Modulation Technology 20

1.5. Non-Imaging Receiver and Imaging Receiver 21

1.6. MIMO-VLC Challenges 24

1.7. Dissertation Organisation 25

Chapter II: Adaptive MIMO-VLC System **27**

2.1. System Model 27

2.2. Illuminance 36

2.3. Decision Feedback Equaliser 39

2.4. Data Rate-Adaptive Modulation 45

2.5. Transmitter Coordination Algorithm 47

2.6. Performance Evaluation 51

Chapter III: Neural Network-Based MIMO-VLC System 60

3.1. Introduction 60

3.2. Pattern Coordination with Neural Network 62

3.3. Initial Tests 64

3.4. Orientation Changes of the Receiver 68

3.5. Receiver with Human Walking Activity Model 74

Chapter IV: Conclusions and Future Work 87

4.1. Conclusions 87

4.2. Future Plan 89

References 92

LIST OF FIGURES

Figure 1. Cisco forecast of global mobile data traffic (source: Cisco VNI Global Mobile Data Traffic Forecast, 2017-2022). 13

Figure 2. Schematic of an basic indoor VLC system [6]. 14

Figure 3. VLC channel and light propagation [7]. 15

Figure 4. Optical spectrum of a phosphor-based white LED (LED OS), the transmission characteristic of the blue filter (BF trans.), and the LED OS after passing through the BF (BF LED OS). Source: Adapted from [11]. 16

Figure 5. Schematic of the receiver. 17

Figure 6. MIMO-VLC system. 20

Figure 7. MIMO-VLC System with: (a) non-imaging receiver, (b) imaging receiver. 22

Figure 8. The arrangement of pointing directions of REs with number of receivers N = 4 in (a) pyramid receiver, (b) hemispheric receiver. Source: Adapted from [42]....24

Figure 9. Configuration of a typical indoor MIMO system with aperture-based receiver. Source: Adapted from [44]. 24

Figure 10. Configuration of a typical indoor VLC MIMO system. 28

Figure 11. Schematic of the indoor VLC MIMO system. 29

Figure 12. Relative geometry between a LED and RE pair. 31

Figure 13. Geometry of the receiver: top view (left) and front view (right). 34

Figure 14. The geometry of a RE with a light source, (a) oblique view, (b) top view [44]. ...36

Figure 15. Top view of the ABR [44]. 36

Figure 16. Illuminance (lux) distribution across the room. 38

Figure 17. Structure of decision-feedback equaliser. 39

Figure 18. Possibility of having an error at every bit index bin of the transmitted data sequence (1000 trails). 43

Figure 19. Schematic of data rate-adaptive technique. 46
Figure 20. Channel condition-based transmitter coordination patterns. 48
Figure 21. Case A: Seven-channel ADR system with adaptive data rate and with Algorithm 1. (a) Distribution of number of channels (b) Distribution of overall data rate (Mbps). 53
Figure 22. Case B: Seven-channel ADR system without adaptive data rate and with Algorithm 1. (a) Distribution of number of channels (b) Distribution of overall data rate (Mbps). 54
Figure 23. Case C: Overall data rate (Mbps) distribution of the seven-channel ADR system without adaptive data rate and with conventional SMP 54
Figure 24. Mean aggregate data rates versus the receiver's distance to the room centre. 55
Figure 25. ABR system with adaptive data rate and with Algorithm 1. (a) Distribution of number of channels (b) Distribution of overall data rate (Mbps). 57
Figure 26. Overall data rate (Mbps) distribution of the ABR system with non-adaptive data rate and SMP. 57
Figure 27. Multi-layer perceptron neural network structure. 61
Figure 28. Architecture of the MLP ANN. 63
Figure 29. Network diagram with backpropagation learning rule. 64
Figure 30. Room A: Mean aggregate data rates versus receiver's distance to the room centre. 66
Figure 31. Room B: Mean aggregate data rates versus receiver's distance to the room centre. 66
Figure 32. Room C: Mean aggregate data rates versus distance to the room centre. 67
Figure 33. Receiver yaw rotation: (a) receiver rotation about z axis in the coordinate system, (b) top view of the receiver with yaw angle ψ 69
Figure 34. Mean aggregate data rate versus distance to the room centre. 70

Figure 35. Receiver roll rotation: (a) receiver rotation about y axis in the coordinate system, (b) front top view of the receiver with roll angle ϕ. 71
Figure 36. Mean aggregate data rate versus distance to the room centre. 73
Figure 37. Mobile device with the seven-channel ADR installed (receiver size not to scale). 75
Figure 38. Orientation of the device: (a) original orientation, (b) yaw rotation around z-aixs, with angle $\phi 1$, (c) roll rotation around y-axis, with angle $\phi 2$, (d) pitch rotation around x-axis, with angle $\phi 3$ [69]. 75
Figure 39. Mean aggregate data rates versus distance to the room centre. 82
Figure 40. (a) Mean aggregate data rates comparison for the CCTC algorithm and the MLP ANN, (b) Difference histogram for the CCTC algorithm and the MLP ANN. 83
Figure 41. (a) Mean aggregate data rates for the water-filling algorithm and the MLP ANN with the difference bar, (b) Difference histogram for the water-filling algorithm and the MLP ANN. 85

LIST OF TABLES

Table I. Parameters 28

Table II. Bit error rate with different training length (with 1000 trails) 44

Table III. Room types in testing phase 65

Table IV. Computing time for MLP ANN and CCTC algorithm 68

Table V. Room types in testing phase 69

Table VI. Computing time for MLP ANN and CCTC algorithm 71

Table VII. Room types in testing phase 72

Table VIII. Computing time for MLP ANN and CCTC algorithm 74

Table IX. Parameters 78

Table X. Parameters 81

Table XI. Testing data sets 82

Table XII. Computing time comparison 86

LIST OF ACRONYMS

ABR: Aperture-Based Receiver

ADR: Angle Diversity Receiver

ANN: Artificial Neural Network

AP: Access Point

BER: Bit Error Rate

CAGR: Compound Annual Growth Rate

CCTC: Channel Condition-based Transmitter Coordination

CNN: Convolutional Neural Network

CSI: Channel State Information

DFE: Decision Feedback Equalisation

FCC: Federal Communications Commission

FEC: Forward Error Correction

FOV: Field of View

GSM: Generalised Spatial Modulation

IEEE: Institute of Electrical and Electronics Engineers

IM/DD: Intensity-Modulation Direct-Detection

ISI: Inter-Symbol Interference

IR: Infra-red

IrDA: Infrared Data Association

JEITA: Japan Electronics and Information Technology Industries Associations

LD: Laser Diode

LED: Light-Emitting Diode

LMS: Least Mean Square

LOS: Line-of-Sight

MIMO: Multiple-Input Multiple-Output

ML: Maximum Likelihood

MLP: Multi-Layer Perceptron

MSE: Mean Square Error

NRZ-OOK: Non-Return to Zero On-Off Keying

OOK: On-Off Keying

ORWP: Orientation-Based Random Waypoint

OWC: Optical Wireless Communications

PDF: Probability Density Function

RE: Receiver Element

RF: Radio Frequency

RNN: Recurrent Neural Network

RV: Random Variable

RX: Receiver

SM: Spatial Modulation

SMP: Spatial Multiplexing

SW-QAM: Square Wave Quadrature Amplitude Modulation

SINR: Signal-to-Interference-plus-Noise Ratio

SISO: Single-Input Single-Output

SNR: Signal-to-Noise Ratio

TX: Transmitter

UV: Ultraviolet

VLC: Visible Light Communications

VLCC: Visible Light Communications Consortium

ZFE: Zero-Forcing Equalisation

CHAPTER I: INTRODUCTION

This chapter gives a brief introduction of wireless communications, visible light communications (VLC), and Multiple-Input Multiple-Output (MIMO) VLC.

1.1. Demand for Wireless Communications

Data traffic transmitted using wireless communications shows an exponential increase. Fig. 1 presents the Cisco forecast of global mobile data traffic, which predicts a 7-fold increase from 2017 to 2022 with a compound annual growth rate (CAGR) of 46%. Mobile data traffic is expected to achieve 77 exabytes per month in 2022. With this massive demand for wireless communication, currently used radio frequency (RF) spectrum resources are becoming exhausted [1]. At the same time, the RF spectrum (from 300 MHz to about 3 GHz [2]) is regulated and heavily supervised by authorities such as the Federal Communications Commission (FCC), and the licensing of the spectrum is also costly. For these reasons, other spectrum bands, such as millimetre and optical wavelengths, are being explored by researchers.



Figure 1. Cisco forecast of global mobile data traffic (source: Cisco VNI Global Mobile Data Traffic Forecast, 2017-2022).

Optical wireless communications (OWC) has a spectrum from 300 GHz to 30 PHz [3], and infra-red (IR), visible light, and ultraviolet (UV) light can be used to carry data. OWC has, therefore, an extensive unlicensed bandwidth. OWC was first explored in the 1960s and 1970s, mainly using infrared wavelengths and laser communication systems [4]. The increasing number of companies providing terrestrial OWC channels makes the OWC market more promising [5]. From the OWC option, visible light communication (VLC) is the research focus of this work and is introduced in detail in the next section.

1.2. Visible Light Communications

Fig. 2 shows the basic schematic of an indoor VLC system. The system consists of a light source, a VLC channel and an optical receiver [5]. VLC uses wavelengths in the visible region of the optical spectrum ranging from 380 nm to 750 nm [3]. The VLC channel, light source and optical receiver are introduced below.

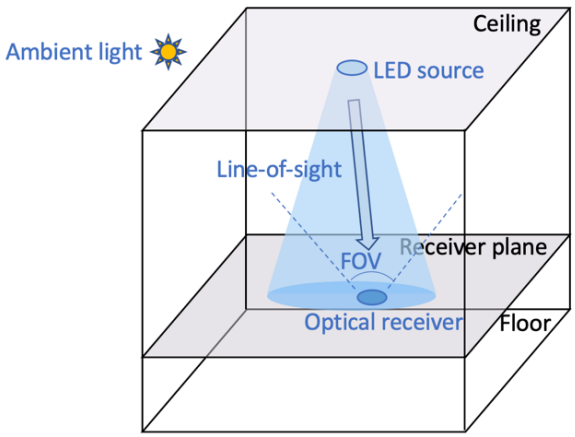
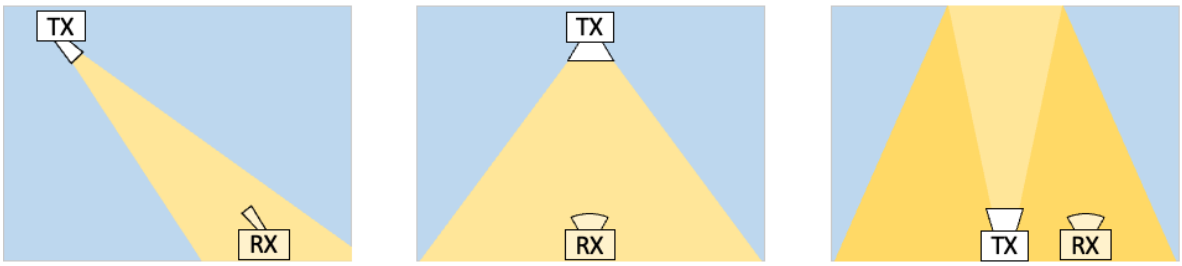


Figure 2. Schematic of an basic indoor VLC system [6].

1.2.1. VLC Channel

A VLC system can work in various scenarios, as set out in Fig. 3. Fig. 3(a) presents the directed Line-of-Sight (LOS) configuration, in which the receiver (RX) and the transmitter (TX) are in direct view of each other, and the directed transmitter emits the light within a small angle. This leads to a higher proportion of the emitted power being received than the case for diffuse

and non-directed LOS geometries. Ultimately this allows a higher data rate link. Fig. 3(b) and Fig. 3(c) show the non-directed LOS light and non-line-of-sight (NLOS) diffused light. The non-directed transmitter emits light on a wide-angle. The NLOS means that the direct view between the TX and the RX is blocked by obstacles, and the transmission is achieved through the reflective paths between the TX and the RX. These two configurations have limitations on the received signal intensity and the achievable data rate.



(a) Directed LOS light (b) Non-directed LOS light (c) Non-directed NLOS light

Figure 3. VLC channel and light propagation [7].

The VLC channel is an intensity-modulation direct-detection (IM/DD) channel. The information is modulated to different light intensity levels at the transmitter and directly detected as intensity levels at the receiver [8].

1.2.2. Light source

Both light-emitting diodes (LEDs) and laser diodes (LDs) can be used as light sources for VLC. LDs can provide higher modulation bandwidth, but care needs to be taken with eye safety, and it is harder to provide homogeneous illumination than LEDs [9]. LEDs are widely used for indoor illumination, and can also be modulated for communications, and therefore LED sources are considered in this thesis. A typical white LED source includes a blue LED and a yellow phosphor coating [10]. The blue photons generated by the LED pass through the yellow phosphor coating either without any conversion or being converted into yellow photons. The combination of the blue and yellow photons is perceived as white light.

Fig. 4 shows the measured spectrum of a single Philips Luxeon Rebel DS64 white LED obtained from a spectrum analyser (Yokogawa, AQ6373) [11]. The wavelength of the blue LED is between 420 nm to 470 nm, and the phosphor emission is between 500 nm to 600 nm. The white LED typically has limited bandwidth because of its high capacitance and large size (compared with the LD). Moreover, the slow response of the yellow phosphor in the LED limits the modulation bandwidth of the LED to approximately 2.5 MHz [12]. Higher bandwidth can be achieved by placing a blue filter at the receiver side. The blue filter transmits the blue portion of the spectrum while blocking the slower yellow portion of the LED spectrum. The black line in Fig. 4 shows the transmission function of a typical blue filter showing that it blocks the slower yellow light. The blue line in Fig. 4 also provides the LED optical spectrum after passing through the blue filter.

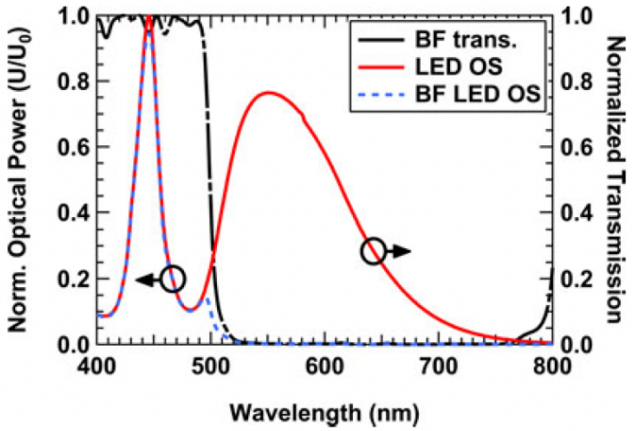


Figure 4. Optical spectrum of a phosphor-based white LED (LED OS), the transmission characteristic of the blue filter (BF trans.), and the LED OS after passing through the BF (BF LED OS). Source: Adapted from [11].

However, the modulation bandwidth is limited to around 14 MHz, even with the blue filter [12]. For an indoor environment with typical illuminance around 400 lux, a VLC channel works at relative low bandwidth and high signal-to-noise ratio (SNR) above 25 dB (see, e.g., [13], [14]).

The LED can be modulated to transmit a data stream and provide light for illumination simultaneously [3]. The optical signal propagates through the channel and is received by the receiver.

1.2.3. Optical receiver

A typical optical receiver includes an optical filter, an optical system, a photodetector, and a pre-amplifier, as shown in Fig. 5 [5]. The optical filter is utilised to mitigate the ambient light noise and prevent the yellow component of the LED from reaching the detector. The optical system is usually an imaging or non-imaging concentrator, which helps to focus the light onto the photodetector. The photodetector generates photocurrent from the received light. Then, an amplifier is used to increase the electrical signal. The optical receiver typically has a field-of-view (FOV) restriction to mitigate the ambient light noise and the potential interference from other LED sources.

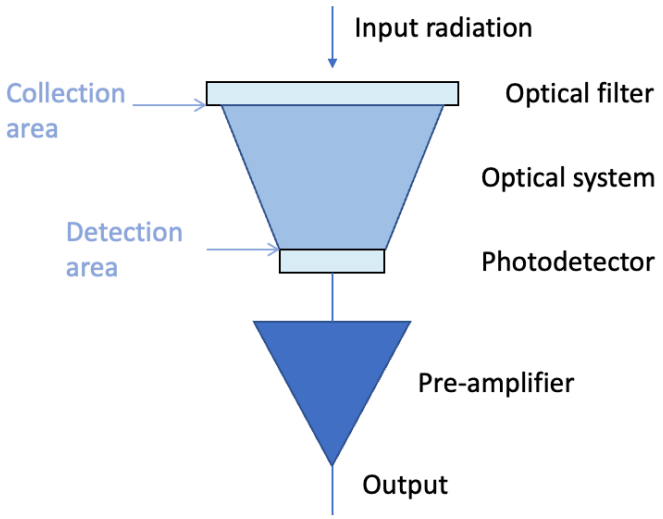


Figure 5. Schematic of a receiver.

Ideally, a receiver is supposed to have a large collection area and a wide FOV [15], which ensures that as much optical power as possible can be collected. The detector size is expected to be small, as a compact structure is easier to implement in devices such as mobile phones and

laptops. A smaller detection area indicates a lower capacitance and a wider bandwidth. However, the concentrator gain G used to achieve these characteristics is limited by the conservation of etendue

$$G = \frac{A_{col}}{A_{det}} = \frac{{n_c}^2}{sin^2(\beta_c)}, \quad (1)$$

where n_c is the ideal optical concentrator refractive index and is typically a constant value for a specific concentrator, β_c is the half-FOV of the receiver, A_{col} is the collection area of the concentrator, A_{det} is the detection area of the photodetector.

Equation (1) shows that there is a trade-off between the collection area and the FOV. When the collection area increases and the detector area is unchanged, the FOV reduces. To overcome the restriction, a receiver design with multiple receivers pointing to different directions can be used. Therefore, a wider FOV can be achieved while keeping a large collection area, and a more significant number of photons can be collected than the single receiver case. The receiver designs which achieve this will be introduced in section 1.4.2.

1.2.4. Literature review and advantages of VLC

Visible light communication (VLC) has been investigated over the last two decades. The idea of indoor VLC utilising LED was first investigated in detail by Tanaka *a* from Keio University in 2000 (see, e.g., [16] and [17]). In 2004, the same group published a paper investigating the influence of reflection, inter-symbol interference and the relation between the data rate and the FOV in the VLC systems, as shown in [18]. Since then, there have been a substantial number of researchers focusing on the development of VLC. Research organisations such as the Visible Light Communications Consortium (VLCC) have been formed [19]. It proposed two standards in 2007, and it is accepted by Japan Electronics and Information Technology Industries Associations (JEITA) as JEITA CP-1221 and CP-1222 [3]. In 2011, the first IEEE 802.15.7 standard was developed for Wireless Personal Area Networks

[20]. In recent years, VLC has become a sizeable active area of research, with a growing number of researchers devoting their effort to develop it (see, for instance, the review papers [21] and [3]).

VLC has several potential advantages. First, it has a broad unlicensed spectrum from 430 THz to 790 THz, which means it can provide additional capacity to mobile communication systems currently dominated by RF communications [3]. Second, VLC can fully utilise the existing LED lighting infrastructure [22]. The VLC system can be established at a lower cost and with less labour than in a situation where no infrastructure exists. Third, the high frequency of visible light cannot penetrate most objects such as walls [3]. An indoor VLC system is immune to interference outside the walls, and it also provides higher security than an RF system within the indoor VLC environment.

1.3. MIMO-VLC System

In most indoor scenarios, there are multiple LEDs on the ceiling to sufficiently illuminate the room, which offers the potential to develop Multiple-Input Multiple-Output (MIMO) VLC systems. MIMO-VLC with multiple transmitters and multiple receivers enables parallel data transmission. The potential higher spectral efficiency offers the possibility of high-speed data communication [1], [2].

A basic pattern of multiple transmitters and multiple receivers was constructed in a wireless optical system in [23], [24], and [25].

Fig. 6 illustrates a general schematic of a MIMO-VLC system [6]. In a typical MIMO-VLC system, the serial input data stream is converted into N_t parallel data streams. The processed N_t signals are emitted by N_t LEDs separately and propagate through the VLC channels. The DC gains of MIMO-VLC channels can be gathered in a $N_r \times N_t$ matrix. At the receiver, the signals are detected by N_r receivers and converted back to a serial data stream.

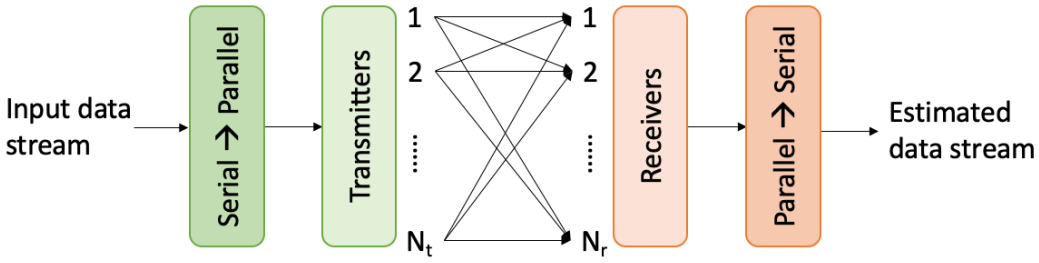


Figure 6. MIMO-VLC system.

MIMO technology is already widely implemented in radio frequency (RF) communication systems where the spectral efficiency is improved by spatial paths with high diversity [26]. However, the available spatial diversity of MIMO-VLC systems is limited by the IM/DD channels. In IM/DD VLC, the small difference in channel gains at the MIMO receivers cannot give a well-conditioned channel matrix, which makes the decoupling of signals difficult. This defect causes multi-stream interference (spatial crosstalk). Techniques to mitigate this crosstalk are introduced in the following sections.

1.4. MIMO-VLC Modulation Technology

The modulation techniques commonly employed in the MIMO-VLC system is introduced in this section, including spatial diversity, spatial multiplexing and spatial modulation [3].

Spatial multiplexing (SMP) assigns independent data streams to each transmitter and transmits them in parallel. Spectral efficiency can be improved by up to the factor of the number of transmitters N_t (see, e.g., [23] and [27]). However, the system performance is suppressed by spatial crosstalk [28]. A variety of SMP systems are reported, including those that employ non-imaging receivers and imaging receivers [29].

Spatial modulation (SM) typically turns on only one transmitter at a time. The index of the transmitter (corresponding to its position) is chosen according to the input data bits. The index is estimated at the receiver side by comparing the detected light intensities for different transmitters and estimating the most likely transmitter. This estimated index is then used to

recapture the transmitted bits. This technique was proposed in [30] and investigated and demonstrated in [30] and [32]. SM improves the spectral efficiency over a single channel by a factor of $\log_2(N_t)$. A variant that enables constellation optimisation is proposed in [33]. Generalised spatial modulation (GSM) was also proposed. It enables the activation of more than one transmitter simultaneously, which improves spectral efficiency but also increases complexity. A scheme that combines the GSM with SMP was introduced in [34].

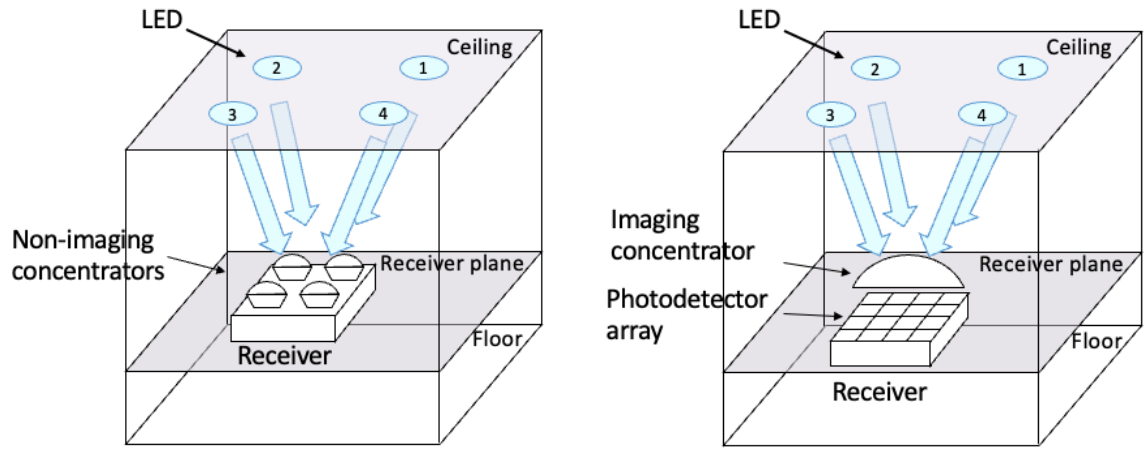
Ganging is another technique to drive multiple LEDs, in which the same data streams are sent from all transmitters. All the signals are received and processed at the receiver side together, as shown in [24] and [12]. Ganging provides limited spectral efficiency as all LEDs transmit the same data (see, e.g., [35]). In a MIMO system, the received signals are hard to decouple at some user locations when the channels are similar. In this situation, enabling ganging can combine similar channels to transmit the same data streams, therefore maintaining a valid communication link.

Precoding can also improve the data rate performance in MIMO-VLC systems. In [36], the data rates are maximised by jointly coordinating the optical power, DC gain, and modulation size. The precoding schemes minimising the mean square error (MSE) and maximising the minimum signal-to-interference-plus-noise ratio (SINR) are also studied in [37] and [38].

1.5. Non-Imaging Receiver and Imaging Receiver

There are two types of receivers employed in the MIMO-VLC systems: non-imaging and imaging receivers. Fig. 7(a) shows a MIMO-VLC system with a non-imaging receiver. Each receiver element (RE) in the non-imaging receiver has its independent non-imaging concentrator. The output is coupled to the photodetector with its own pre-amplifier. Each receiver can detect different light intensity levels from different sources. Fig. 7(b) shows a MIMO-VLC system with an imaging receiver. The imaging receiver uses a single optical

element to collect and focus the light sources onto a detector array with many pixels, according to the angle of arrival of the light from the source. Every pixel on the photodetector array is a receiver channel and has its individual pre-amplifier so that each channel can have high bandwidth. Because different light sources have different angles of arrival to the receiver, they can be separated and detected by different detectors [39].



(a) (b)

Figure 7. MIMO-VLC System with: (a) non-imaging receiver, (b) imaging receiver.

There is a trade-off between the performance of two receivers. The non-imaging receiver is bulkier than the imaging one. However, it is hard to select a proper detection array of the imaging receiver which adapts to the system. Moreover, with the improvement of the diversity of the non-imaging receiver, its FOV can be much higher than that of the imaging receiver.

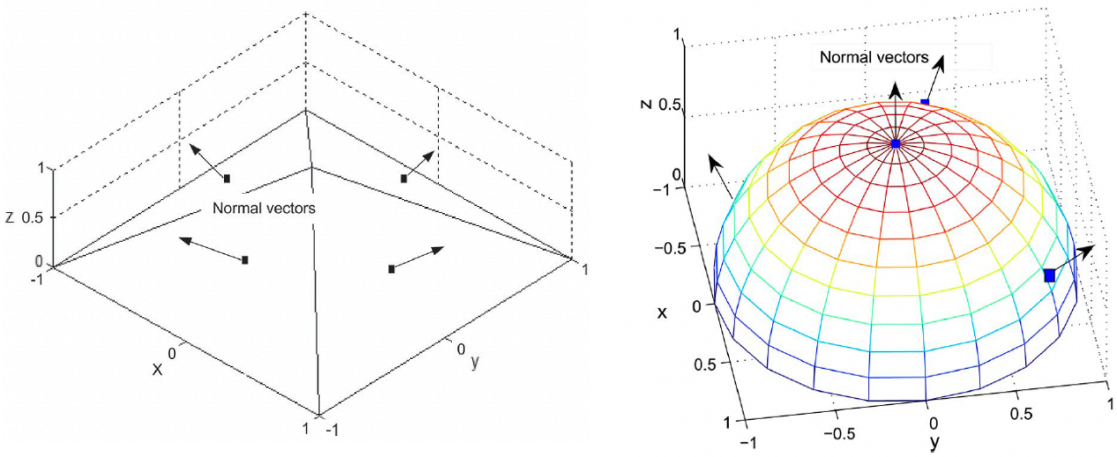
The non-imaging receiver can achieve a very wide FOV by using receiver designs with higher diversity. Spatial correlation can also be decreased by the enhanced power difference (diversity) of the received signals [40]. A variety of receiver designs have been developed to achieve high diversity.

The spatial diversity receiver was explored to reduce spatial correlation (see, e.g., [6] and [31]). Although this receiver has a limitation in IM/DD systems because the received signal

power changes slowly when varying the receiver position [41], variants have been invented to solve the problem. Reference [24] shows a link-blocked receiver using the opaque screen(s) to block one or several link(s) to reduce channel correlation in a MIMO system. In this case, the improvement in the channel conditions and BER performance outweighs the loss of the received energy.

The angular diversity receiver has also been investigated by researchers. Typically, a single receiver has a limited FOV constrained by the required detection area and the detector bandwidth because of the conservation of etendue, as mentioned in section 1.2.3. The angular diversity receiver achieves high diversity by pointing multiple receivers in different directions to have a wide FOV overall. Differentiating the receiver angles ensures higher diversity, more identifiable power differences and compact structure of the system compared with that of the spatial diversity receiver. Different designs and configurations of REs have been proposed, including a pyramid receiver and hemispheric receiver [42]. Fig. 8 shows that the pointing directions of REs of the pyramid receiver and the hemispheric receiver are arranged according to the normal vectors on the surfaces of a pyramid and a hemisphere. One challenge with the angular diversity receiver is to integrate multiple REs that are not planar, which leads to bulky systems (see, e.g., [43] and [42]). Reference [44] proposes the aperture-based receiver (ABR), which uses only planar elements. An example of this approach can be seen in Fig. 9. Each RE in the ABR has an aperture and a bare photodetector. Angular diversity is achieved by arranging an aperture above each photodetector to make sure photodetectors only receive the light with specific angles relative to the LED and the aperture. The proposed ABR achieves high angular diversity with a compact planar structure. The ABR does not have an optical concentrator, so it has a theoretically wider FOV than the typical angle diversity receiver of the same size. However, the ABR does not have concentrator gain, which means it requires large detection areas. The ABR can also receive more ambient light noise from all directions,

which can reduce its performance. Different designs of the angular diversity receivers are investigated later in section 2.1.4.



(a) (b)

Figure 8. The arrangement of pointing directions of REs with number of receivers N = 4 in (a) pyramid receiver, (b) hemispheric receiver. Source: Adapted from [42].

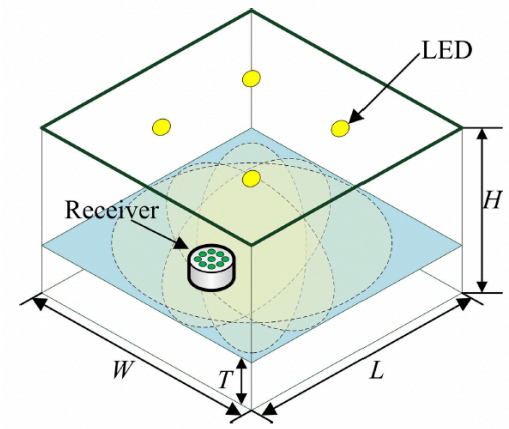


Figure 9. Configuration of a typical indoor MIMO system with aperture-based receiver. Source: Adapted from [44].

1.6. MIMO-VLC Challenges

The primary challenges that need to be explored in MIMO-VLC systems are summarised below. First, although a VLC system can shield interference outside the walls of the room in

which the system is situated, the multiple LEDs inside an indoor environment may cause multi-stream interference between them. The decreased SINR caused by the interference degrades system performance. Second, band-limited VLC channels also cause inter-symbol interference (ISI) during high-speed communications. Third, the receiver design affects the system performance. The structure of the receiver affects the received interference and SINR of each channel. The selection of proper devices with imaging or non-imaging optics also affects the system FOV, determining the speed and energy consumption of the system [45]. Furthermore, the eye safety issue also should be considered because the LEDs need to provide illumination [46].

1.7. Dissertation Organisation

Chapter I provides an outlook on basic knowledge, literature and challenges of the VLC and MIMO-VLC systems that lay out the research background. In the following chapters, the work is focused on solving these challenges in a static environment to create high-speed MIMO-VLC downlinks.

The outline of the following chapters is introduced below:

- Chapter II demonstrates an adaptive indoor MIMO-VLC system considering data rate-adaptive modulation and transmitter pattern coordination algorithm. The system also employs two types of diversity receiver, zero-forcing MIMO equalisation, and decision-feedback equalisation, to mitigate spatial crosstalk and temporal crosstalk. In the new adaptive system, high-speed downlink communication systems with 676 Mbps and 434 Mbps peak data rates are achieved separately with the ADR and the ABR. The peak data rate of the ADR-based system is 56 per cent higher than that of the ABR-based system. The new systems also reach 41 per cent and 127 per cent data rates improvements (on

average) compared with a conventional spatial multiplexing scheme with the ADR and the ABR, separately.

- Chapter III employs a neural network in the indoor MIMO-VLC system to replace the algorithm proposed in Chapter II, which efficiently decreases the computational complexity of the constructed system. The neural network can successfully predict the optimal transmitter patterns and up-sampling factors for the indoor MIMO-VLC system with varying receiver positions and orientations. Moreover, the water-filling algorithm is employed as a benchmark with the optimal data rate compared with the neural network approach. The neural network shows its potential as a straightforward technique with one third in computing time compared with the water-filling algorithm.
- Chapter IV concludes the thesis and summarises the achievements of the proposed adaptive MIMO-VLC system. Future work and developments related to the proposed system are also discussed.

CHAPTER II: ADAPTIVE MIMO-VLC SYSTEM

This chapter introduces a high-speed indoor MIMO-VLC system model with transmitter coordination algorithm and data rate-adaptive modulation. At each user location across the room, the number of MIMO transmission channels is varied by allocating different transmitters to one or several group(s) and sending the same data stream in each group. Then, the data rate of each channel group is separately optimised. The proposed adaptive scheme is compared with the spatial multiplexing scheme, using two receiver designs: a seven-channel angular diversity receiver (ADR) and an aperture-based receiver (ABR). The system also compares the ADR and ABR under the proposed scheme. Moreover, the illuminance of the room is analysed.

2.1. System Model

Fig. 10 shows a schematic of a typical indoor MIMO-VLC system [6]. N_t LEDs are installed on the ceiling, illuminating the room as well as transmitting information to the receiver. A receiver with N_r receiver elements (RE) is implemented on the receiver plane. Each of them has a non-imaging concentrator and is oriented in a different direction. Each RE receives the light from multiple LEDs but with different light intensities. The channels between N_t transmitters and N_r REs construct a $N_r \times N_t$ channel matrix, $\boldsymbol{H}$. It is assumed that the LEDs are operated by a controller. The parameters used for simulation are shown in Table I [6].

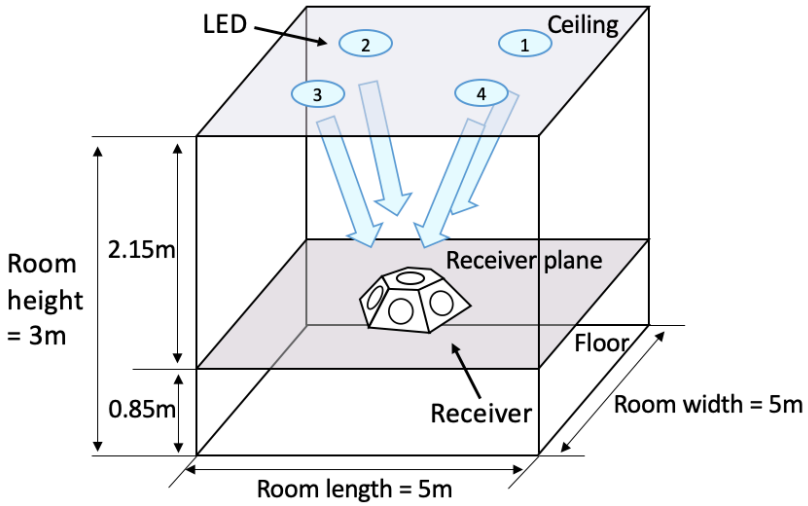


Figure 10. Configuration of a typical indoor VLC MIMO system.

Table I. Parameters

Parameters	**Values**
Room size (width × length × height)	5m × 5m × 3m
Receiver plane height	0.85m
Numbers of LEDs (N_t)	4
Modulation power per LED (P_{LED})	1W
LED pitch	2.5m
Lambertian order (m) (transmitter semi-angle ($\theta_{1/2}$))	1 (60°)
LED and Receiver bandwidth	8.4MHz [6]
Concentrator refractive index (n_c)	1.5
Collection area per RE (A_j)	100 mm^2
Half-angle FOV (β_c) per RE	33°
Detector responsivity (ρ)	0.4A/W [6]

Parameters	Values
Pre-amplifier noise current density (i_{amp})	5pA/Hz$^{1/2}$ [6]
Ambient light photocurrent density ($\gamma_{ambient}$)	10.93A/(m^2·Sr) [47]

The schematic of the system model is shown in Fig. 11, which will be explained in detail in the following sections.

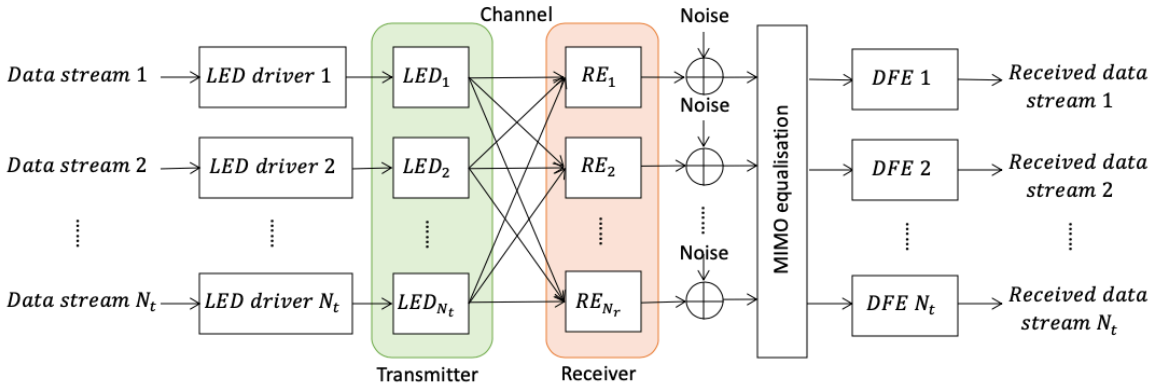


Figure 11. Schematic of the indoor VLC MIMO system.

2.1.1. Transmitter

The transmitter includes N_t LEDs on the ceiling, pointing vertically downwards. White LEDs are used to illuminate the room and provide communications. As mentioned in Chapter II, the white light is generated by a blue LED with a phosphor coating. The slow time response of the yellow phosphor limits the LED switching speed to approximately 2.5 MHz [12]. The improved modulation bandwidth can be obtained by employing a blue filter at the receiver side, ensuring only the blue emission component of the LED is detected by the receiver, as mentioned in section 1.2.2. The improved LED bandwidth is set as 8.4 MHz, the same as the receiver bandwidth given in [6].

The LEDs are modelled as Lambertian sources. The Lambertian source order m can be derived from the LED semi-angle $\theta_{1/2}$ at half power

$$m = \frac{\ln\left(\frac{1}{2}\right)}{\ln\left(\cos\left(\theta_{1/2}\right)\right)}. \tag{2}$$

In this work, 4 LEDs are arranged as a 2×2 array with a 2.5 m pitch between the adjacent LEDs. A Non-Return to Zero On-Off Keying (NRZ-OOK) modulation scheme is used to transfer data. The binary data streams are converted to electrical signals, which modulate the intensity of the LEDs. Each electrical signal is convolved with the impulse response of LED when it passes through the LED [48]

$$h_{LED}(t) = e^{-\omega_c t}, \tag{3}$$

where ω_c is the 3dB cut-off bandwidth of the LED in units of angular frequency. After the LED, the vector $\boldsymbol{D} = [d_1, \dots d_i \dots, d_{N_t}]^T$ is obtained at each time instance. d_i represents the convolution of the ith data stream and the impulse response of the ith LED. T presents the transpose of the matrix.

2.1.2. Channel Matrix between Transmitters and Receivers

$\boldsymbol{H}$ is the $N_r \times N_t$ channel matrix

$$\boldsymbol{H} = \begin{bmatrix} h_{11} & \dots & h_{1i} & \dots & h_{1N_t} \\ \vdots & \ddots & \vdots & & \vdots \\ h_{j1} & \cdots & h_{ji} & \dots & h_{11} \\ \vdots & & \vdots & \ddots & \vdots \\ h_{N_r1} & \cdots & h_{N_ri} & \dots & h_{N_rN_t} \end{bmatrix}, \tag{4}$$

where h_{ji} shows the DC gain between ith LED and jth RE. h_{ji} is given as

$$h_{ji} = \begin{cases} \frac{(m+1)A_j}{2\pi {d_{ji}}^2} cos^m(\alpha_{ji}) cos(\beta_{ji}) & 0 \le \alpha_{ji} \le \frac{\pi}{2} \; and \; 0 \le \beta_{ji} \le \beta_c \\ 0 & otherwise \end{cases}, \tag{5}$$

where A_j is the collection area of the jth RE, d_{ji} is the distance between the ith LED and the jth RE, α_{ji} is the irradiance angle at ith LED to jth RE, β_{ji} is the incident angle at jth RE to ith LED, β_c is the receiver half-angle field-of-view (FOV).

In order to obtain α_{ji} and d_{ji}, three vectors between ith LED and jth RE are defined, as shown in Fig. 12 [42].

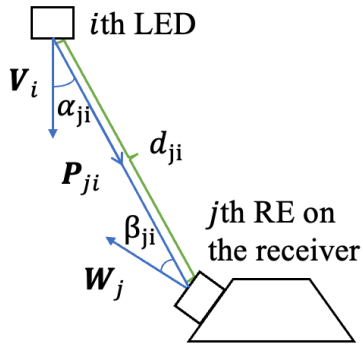


Figure 12. Relative geometry between a LED and RE pair.

In Fig. 12, $\boldsymbol{V}_i$ is the normal vector of ith LED, pointing vertically downwards, $\boldsymbol{W}_j$ is the normal vector of jth RE, $\boldsymbol{P}_{ji}$ is the vector pointing from ith LED to jth RE. Here α_{ji} and β_{ji} can be derived as

$$\alpha_{ji} = \cos^{-1}\left(\frac{\boldsymbol{V}_i \cdot \boldsymbol{P}_{ji}}{\|\boldsymbol{V}_i\|\|\boldsymbol{P}_{ji}\|}\right), \tag{6}$$

$$\beta_{ji} = \cos^{-1}\left(\frac{\boldsymbol{P}_{ji} \cdot \boldsymbol{W}_j}{\|\boldsymbol{P}_{ji}\|\|\boldsymbol{W}_j\|}\right). \tag{7}$$

Only the line-of-sight (LOS) link is considered in the system model because LOS is the primary communication link with most power transmitted.

2.1.3. Receiver

The signal received by REs at a time instant is given by

$$\boldsymbol{R} = \rho P_{LED}(\boldsymbol{HD}) + \boldsymbol{i}_N \,, \tag{8}$$

where $\boldsymbol{R} = [r_1, \dots r_j \dots, r_{N_r}]^T$, ρ is detector responsivity, $\boldsymbol{i}_N = [i_{n,1}, \dots i_{n,j} \dots, i_{n,N_r}]^T$ is the noise current vector referred to the input of the pre-amplifier. $i_{n,j}$ for each RE is an independent identically distributed (i.i.d.) AWGN random variable [42]. The transmission of the blue optical filter is assumed to be 100% and is not shown in the equation.

P_{LED} is the modulation power per LED [6]. When transmitting data streams using OOK, 0 and 1 are transmitted by modulating the intensity of the LED light emission. The optical signals are emitted from the LEDs and propagate through the VLC channels (represented as $P_{LED}(\boldsymbol{H} \cdot \boldsymbol{D})$). The REs detect different light intensity levels and convert these to electrical signals, with additional noises (defined as $\boldsymbol{R}$).

The propagation, detection and amplification of the signal process introduce optical signal noise, ambient noise, and amplifier noise. The signal and ambient noise are the shot noise from the desired signal and the detection, while the amplifier noise involves all the thermal and shot noise relevant to the pre-amplifier circuit [49]. The noise variance is calculated from the mean square of the noise current

$$\overline{i_{n,j}^2} = 2e\big(i_{signal,j} + i_{ambient,j}\big)B + i_{amp}^2 B \,, \tag{9}$$

where e is the elementary positive charge, i_{amp} is the pre-amplifier noise current density and B is the bandwidth of the receiver. $i_{signal,j}$ is the average received current density for the jth RE

$$i_{signal,j} = \rho P_{LED} \sum_{i=1}^{N_t} h_{ji}\, d_i \,, \tag{10}$$

$i_{ambient,j}$ represents received current density from ambient light for jth RE

$$i_{ambient,j} = \gamma_{ambient} A_j 2\pi(1 - \cos(\beta_c)) \,, \tag{11}$$

where $\gamma_{ambient}$ is the ambient light photocurrent per square meter per steradian, $2\pi(1-\cos(\beta_c))$ is the solid angle of a cone corresponding to the cross-section with the angle $2\beta_c$.

A linear zero-forcing equalizer (ZFE) is applied as the de-multiplexing technique to decouple the matrix. The estimated vector $\widehat{\boldsymbol{D}}$ of the transmitted signals can be obtained by

$$\widehat{\boldsymbol{D}} = \boldsymbol{H_{ZF}R}\,, \tag{12}$$

where

$$\boldsymbol{H_{ZF}} \stackrel{\text{def}}{=} (\boldsymbol{H}^*\boldsymbol{H})^{-1}\boldsymbol{H}^*\,, \tag{13}$$

denotes the Moore-Penrose inverse of $\boldsymbol{H}$, which gives the best approximate solution for non-squared matrices and non-full rank square matrices [42]. $\boldsymbol{H}^*$ is the conjugate transpose of $\boldsymbol{H}$. For the linear equation (8), (13) helps to find the vector $\widehat{\boldsymbol{D}}$ such that the Euclidean norm $\left\|\rho P_{LED}\left(\boldsymbol{H}\widehat{\boldsymbol{D}}\right) + \boldsymbol{i}_N - \boldsymbol{R}\right\|$ is minimised [50].

Decision-feedback equalisation (DFE) is employed to overcome inter-symbol interference after the MIMO demultiplexing [51]. This process effectively uses excess signal-to-noise ratio (SNR) to increase bandwidth and hence data rate. Each channel (or channel group) has its own DFE separately optimised. During the operation, a training mode is used at first to optimise the weighting coefficients of DFEs. The actual data streams are processed by the DFEs after the DFEs are well-trained.

2.1.4. Angular Diversity Receiver Design

In this work, two types of angular diversity receiver design are analysed.

A. Angle Diversity Receiver

As mentioned in section 1.4.2, the angular diversity receiver provides a simple and efficient method to reduce the spatial correlation between channels and enlarge the FOV of the receiver. The different directions of each RE in the angular diversity receiver ensures each RE has a high

power difference. The number of REs is typically more significant than the number of transmitters, and this approach makes the decoupling of the received signal in (13) more effective. More REs typically ensures a wider FOV.

Fig. 13 shows a seven-channel angle diversity receiver (ADR) design. The top view of the ADR shows 6-fold rotational symmetry, and the angle between adjacent REs is 60°. From the front view, the pointing direction of RE 1 to 6 has an upward angle of 30° relative to the horizontal receiver plane. RE 7 points vertically upwards. Such a receiver was implemented in the hOME Gigabit Access project (OMEGA) [52].

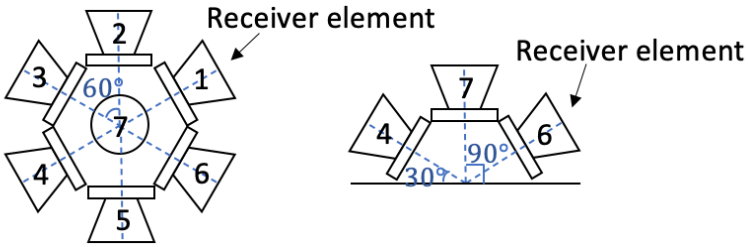


Figure 13. Geometry of a ADR: top view (left) and front view (right).

Each RE consists of a non-imaging concentrator to gather the radiation, a photodetector to convert optical power to the photocurrent, and a pre-amplifier to amplify the signal. The receiver collection area is given by

$$A_j = \frac{{n_c}^2}{sin^2(\beta_c)} A_{det}\,, \tag{14}$$

where n_c is the ideal optical concentrator refractive index, A_{det} is the detection area of the photodetector.

The collection area A_j of each RE is 100 mm^2. The half-angle FOV (β_c) of each RE is 33°, limiting the number of transmitted signals each RE can receive, thus reducing the spatial crosstalk.

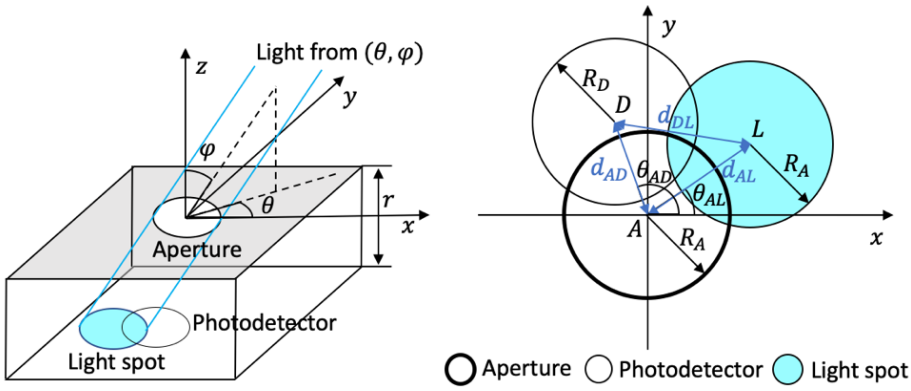
Because of the small distances between each RE (compared with the distances between LEDs and REs), it is assumed that the location of the REs is at the same point.

B. Aperture-Based Receiver

The aperture-based receiver was introduced in section 1.4.2 as a compact and simple design to reduce the spatial correlation between the received signals and enlarge the FOV of the receiver. In this section, an ABR, as proposed in [44], will be introduced in detail. The receiver consists of N_r REs. Each single RE is composed of a bare photodetector and an aperture above it. The photodetector and aperture are located on two parallel planes with a vertical distance r, as shown in Fig. 14(a). The aperture is made on an opaque screen, from which the light can pass through and form a light spot on the photodetector plan. The light direction is represented by the angle of incidence φ and the polar angle θ. In this work, the ABR is assumed to have the same bandwidth as the ADR.

Fig. 14(b) is the top view of a RE. R_A is denoted as the radius of the aperture and R_D is denoted as the radius of the photodetector. In this work, the assumption $R_A = R_D = r$ is made. The light spot has the same size as the aperture because the light propagates in parallel, and the relative positions among aperture, light spot and photodetector are not fixed. The relative position between the light spot and aperture is represented by the radial distance d_{AL} and the polar angle θ_{AL}. The relative position between the aperture and the photodetector is denoted by the radial distance d_{AD} and the polar angle θ_{AD}. The distance between the light spot and the photodetector is d_{DL}. To compare the ADR and the ABR, the detection area A_{det} of each RE in the ABR is set to 100 mm^2, which is the same as the collection area of the RE in the ADR. The half-angle FOV (β_c) of each RE in ABR is 45°, larger than that employed in the ADR (30°). The FOV is restricted by the non-imaging concentrator. For the ABR, the relative position between the aperture and the photodetector limits the maximum acceptable incident angle of the light for the ABR, which sets the achievable FOV. The FOV of the ABR is

calculated from $\arctan(\frac{d_{AD}}{r})$, which is the largest possible angle that the photodetector will overlap with the light spot.



(a) (b)

Figure 14. The geometry of a RE with a light source, (a) oblique view, (b) top view [44].

Fig. 15 shows the top view of a configuration of the receiver with eight REs. The assumption is made that the positions of eight REs are at a single point of O'. The angular diversity of the system is realised by the different relative positions of each photodetector and aperture pair.

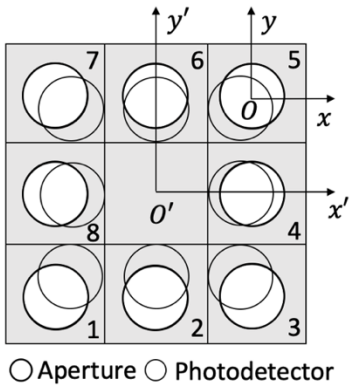


Figure 15. Top view of the ABR [44].

2.2. Illuminance

As mentioned in section 2.1, room lighting is the primary purpose of the LED, so the LEDs should emit sufficient power to illuminate the room and adequate modulation power to transmit information. In operation, the LEDs are set to a fixed average illuminance as required for

lighting and modulated around this level for communications. This section investigates the optical power needed to illuminate the room, as this indicates how much communications power will be available given a particular modulation depth.

2.2.1. System Model

The horizontal illuminance directly from ith LED to a point (x, y, z) on the receiver plane is

$$E_{hor,i} = \frac{I(\alpha_i)cos(\beta_i)}{{d_i}^2}, \tag{15}$$

where d_i is the distance between ith LED and a point (x, y, z) on the receiver plane, $I(\alpha_i)$ is the luminous intensity of the ith LED source and α_i is the irradiance angle, β_i is the incident angle for the illuminated surface, which equals α_i when the surface is horizontal.

The horizontal illuminance from all LEDs to a point (x, y, z) on the receiver plane is

$$E_{hor} = \sum_{i=1}^{N_t} E_{hor,i}\,. \tag{16}$$

To obtain $E_{hor,i}$, the luminous intensity $I(\alpha_i)$ is required. The luminous intensity of the ith LED source is

$$I(\alpha_i) = I(0)cos^m(\alpha_i)\,, \tag{17}$$

where m is the Lambertian index of the LED, $I(0)$ is the on-axis luminous intensity of the LED

$$I(0) = \frac{(m+1)\Phi}{2\pi}, \tag{18}$$

where Φ is the luminous flux, showing the intensity of the light as perceived by the human eye [53]. The luminous flux can be obtained from

$$\Phi = \eta_{LER} P_{LED}\,, \tag{19}$$

where η_{LER} is the luminous efficacy of radiation. An ideal white LED can have a luminous efficacy of radiation between 250-370 lm/W [54]. P_{LED} is the LED optical power (radiant power).

2.2.2. Results

The system settings can be found in section 2.1, with parameters provided in Table I. The LED optical power is calculated based on the required illuminance range.

The resulting illuminance in the room is shown in Fig. 16. The figure shows the illuminance distribution on the receiver plane. In the proposed system, when the room has an average horizontal illuminance of around 430 lux, each LED can be 14.6 to 21.6 W (corresponding to the luminous efficacy of radiation 370 lm/W to 250 lm/W as mentioned in section 2.2.1). This illuminance satisfies the desired levels of 300 to 750 lux for an office environment set out in the international standard [55]. In addition, the required illumination power is much higher than the modulation power, which means the modulation will not affect the room illumination.

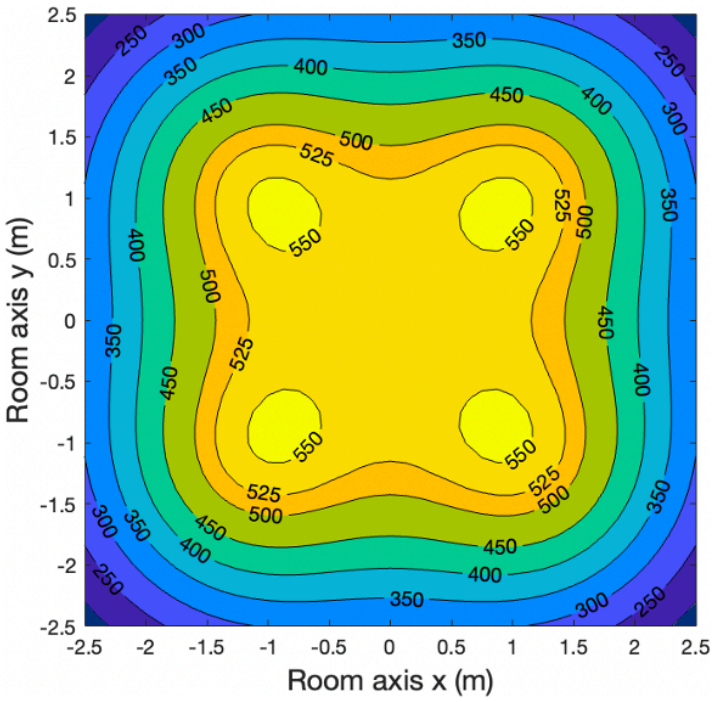


Figure 16. Illuminance (lux) distribution across the room.

2.3. Decision Feedback Equaliser

2.3.1. Decision Feedback Equalisation

High data rate communications with the limited bandwidth LED channels leads to temporal crosstalk (ISI) between adjacent communication symbols. Applying a decision feedback equaliser (DFE) is a typical method to overcome ISI and achieve a high data rate [56]. In this section, the structure and features of DFE are studied.

The principle of DFE is that when the interference is induced from previous symbols to the current symbol, the ISI can be estimated and cancelled after detecting and decide the previous symbols [57].

Fig. 17 shows a DFE structure established in the direct transversal form [58].

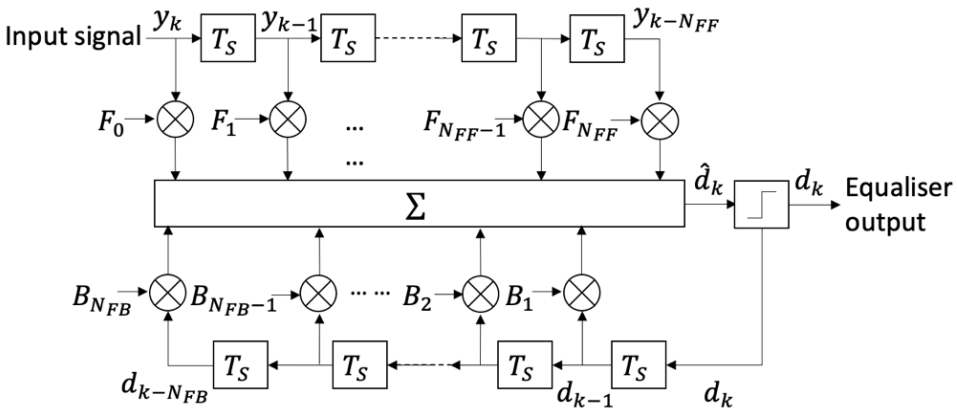


Figure 17. Structure of decision-feedback equaliser.

The system consists of a transversal feed-forward filter and a transversal feedback filter. T_S is delay tap. The output of the system $\hat{d}_k$ is expressed as

$$\hat{d}_k = \sum_{m=0}^{N_{FF}} F_m(k) y_{k-m} + \sum_{n=1}^{N_{FB}} B_n(k) d_{k-n}\,, \tag{20}$$

where $\boldsymbol{F}_k = \left[F_0(k)\ F(k)_1\ \ldots\ F_{N_{FF}}(k)\right]$ are weighting coefficients (tap gains) for the feed-forward filter at time instant k and $\boldsymbol{B}_k = \left[B_1(k)\ B_2(k)\ \ldots\ B_{N_{FB}}(k)\right]$ are weighting coefficients

(tap gains) for the feed-back filter. $\boldsymbol{y}_k = [y_k\ y_{k-1} \ldots\ y_{k-N_{FF}}]$ is the input signal to the equaliser. The previous decisions $d_{k-1}, d_{k-2} \ldots\ d_{k-N_{FB}}$ are fed back into the DFE. d_k at time instant k can be obtained after making a decision on the detected signal $\hat{d}_k$.

DFE needs an algorithm to update the weighting coefficients (filter tap gains) $\boldsymbol{F}_k$ and $\boldsymbol{B}_k$ to their optimum values, and the least mean square (LMS) is employed here [58]. By using the LMS algorithm, the vector $\boldsymbol{F}_k$ and $\boldsymbol{B}_k$ are continuously updated in each iteration until the minimum mean square error (MSE) $e(k)$ is obtained, as shown below

$$\boldsymbol{W}_{k+1} = \boldsymbol{W}_k + \mu e(k)\boldsymbol{Y}_k\,, \tag{21}$$

where

$$\boldsymbol{W}_k = [F_0(k)\ F_1(k) \ldots\ F_{N_{FF}}(k)\ B_1(k)\ B_2(k) \ldots\ B_{N_{FB}}(k)]\,, \tag{22}$$

$$\boldsymbol{Y}_k = [y_k\ y_{k-1}\ \ldots\ y_{k-N_{FF}}\ d_{k-1}\ d_{k-2} \ldots\ d_{k-N_{FB}}]\,, \tag{23}$$

and μ is the step size. $e(k)$ is the error, which is defined in two modes.

The first mode is the training mode shown as

$$e(k) = d_{training,k} - \hat{d}_k\,, \tag{24}$$

where $d_{training,k}$ is a known training sequence transmitted through the equaliser. The error is calculated from the difference between the detected signal $\hat{d}_k$ and the known training sequence.

The second mode is the decision-directed mode

$$e(k) = d_k - \hat{d}_k\,, \tag{25}$$

where the error is calculated from the difference between the estimated d_k and the DFE output $\hat{d}_k$. The decision-directed mode keeps updating the weighting coefficients of the filter when the transmitted data is unknown.

The decision-directed mode has a higher possibility of making wrong decisions than the training mode, making it harder to reach the minimum MSE and get the optimal weighting coefficients than the training mode. The reason is that the training mode employs a known training sequence value to obtain the error in (24) and optimise the weighting coefficients in (20). The decision-directed mode employs the estimated training sequence value obtained from maximum likelihood detection to calculate the error in (25) and optimise the weighting coefficients in (20). The accuracy and tracking ability of the training mode is superior to that of the decision-directed mode.

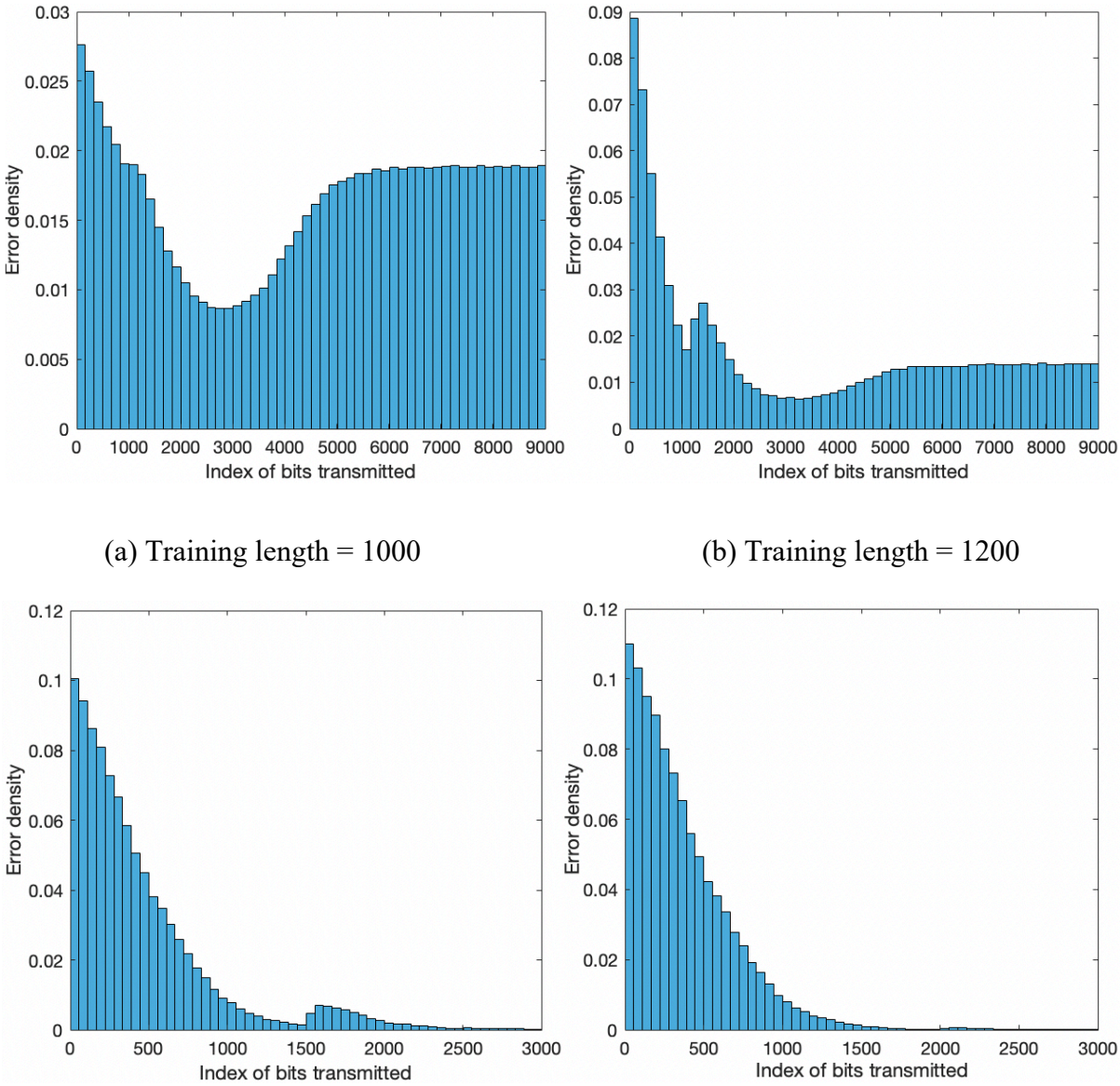
2.3.2. DFE Step Size and Training Length Optimisation

The DFE step size and training length need to be determined. A Single-Input Single-Output (SISO) system is employed to explore the relationships among the DFE step size, training length and other system settings. The system parameters employed are those used for the seven-channel ADR in Table I in section 2.1, except that there is only one LED at (-1, -1, 3) and one RE pointing upwards at (1.25, 1.25, 0.85). The data rate is 120 Mbps, and each packet contains 20000 bits.

Step size μ is one critical parameter affecting the DFE performance. A larger step size leads to stronger tracking ability and higher convergence rate but also excess noise [57]. The step size is a constant value in the standard LMS algorithm [59]. An optimal step size of 0.01 was obtained by testing the possible values between 0 and 1 in the simulation. The DFE gives the best result with this value for the step size in the proposed system. The step size value is affected by the data rate and not by the training length. In addition, the optimal value of the step size shows observable changes only when the data rate varies drastically. When the data rate is around hundreds of megabits per second, the optimal step size obtained is expected to be unchanged.

Once the step size is obtained, the relationship between the data sequence length to train the DFE and the performance of the DFE is investigated. In the experiment, different lengths of the training sequence are tested, and the DFE performance is assessed by the resulting number of errors in the employed SISO system. At first, the DFE works with known training data in the training mode. The DFE is allowed to switch from the training mode to the decision-directed mode with unknown data. The weighting coefficients of the DFE is not fixed during the experiment. If the known training length is sufficient, the weighting coefficients can be optimised during the training mode, and it will not change too much when the equaliser switches to the decision-directed mode, leading to a stable error. This provides a valuable indicator of whether the training sequence is long enough.

The error density distribution of the transmitted data collected from 1000 trials is shown in Fig. 18. The y-axis represents the possibility of having an error within the bit index bin range from all the bit indexes. The x-axis indicates the bit index of the data sequence. The x-axis in Fig. 18 only shows the range from 0 to where the error trend remains almost unchanged (9000 bits or 3000 bits), as beyond this point to the end of the training sequence, the corresponding errors are constant.



(a) Training length = 1000

(b) Training length = 1200

(c) Training length = 1500

(d) Training length = 2000

Figure 18. Possibility of having an error at every bit index bin of the transmitted data sequence (1000 trails).

Taking the 1200 training bits case in Fig. 18(b) as a typical example, it is clear that the error density tends to decrease at the beginning. However, it increases again after 1200 bits. After that, the error density drops and rises after 3000 bits. Finally, the error density becomes stable at an undesirable high value after 5000 bits, which shows that the DFE does not reach its optimal performance. Within the first 1200 known training bits, the DFE uses the training mode, and the weighting coefficients converge to their optimal values. After 1200 bits, there is no

known training data transmitted through the equaliser, and the system switches from training mode to decision-directed mode. Without enough known training bits, the DFE loses the high tracking ability to converge to its optimal weighting coefficients, which stops it to achieve its best performance at the end. The same trend happens after 1500 bits in Fig.18(c). Fig. 18(d) shows that the error density converges stably when the training length is longer than 2000 bits, which means the DFE is well-trained in this circumstance.

The relationship between the bit error rate (BER) of the whole system and training length is provided in Table II. The BER is calculated from the total number of errors divided by the total number of transmitted bits. The BER value reduces substantially when the number of training bits is increased from 1000 to 2000. The BER then stabilises at a substantially reduced level when the training length is longer than 2000 bits. The standard BER $\leq 1\times10^{-3}$ is employed here, as this is a commonly accepted level for error correction [60]. Table II shows that the training sequences with training bits longer than 2000 will have BER satisfying this benchmark after cutting off the first 5000 bits. In this system, a sequence of 2000 training bits is suitable because continuously increasing training length does not substantially improve the BER.

Table II. Bit error rate with different training length (with 1000 trails)

Training bits	**BER**	**BER (cut off the first 5000 bits)**
1000	0.3059	0.3240
1200	0.0788	0.0730
1500	0.0138	0.0030
1800	0.0112	5.2624e-04
2000	0.0106	3.7383e-05
3000	0.0106	3.6242e-05
5000	0.0106	3.4228e-05

The experiment shows that each DFE has a threshold (optimal) training length to ensure it is well-trained. The BER cannot achieve its optimal value when the training length is shorter than the optimal length but does not improve substantially when the training length is longer than the optimal length.

2.4. Data Rate-Adaptive Modulation

In an indoor MIMO-VLC system, different transmitters typically have the same data rate (such as in the case of the model in [6]). However, with multiple channels in the system, some channels are affected by higher interference in some specific receiver locations. These channels can have much higher BER than other high-quality channels. A good channel is expected to achieve a higher data rate than a poor channel with the same BER requirement. In this circumstance, having adaptive data rates depending on the channel condition can ensure each channel reaches its optimised data rate.

Here a data rate-adaptive modulation technique is proposed. The basic idea behind data rate-adaptive modulation is to achieve the time-alignment of waveforms by adjusting the up-sampling factor U_f of each channel based on the desired data rate. Fig. 19 is a simple schematic representing the mechanism behind the data rate-adaptive technique. Two waveforms represent signals from two sources within the packet duration t_{packet}. The sample period T_{sample} is identical in all channels, and the total number of samples N_{sample} also matches. The data rate of waveform 2 is twice as fast as waveform 1. In this circumstance, the up-sampling factor of the high data rate signal is half of the up-sampling factor of the low data rate signal. Hence the waveforms with different data rates remain time-aligned throughout the packet time, and the overall time spent on transmitting the packets with different lengths is the same for all channels.

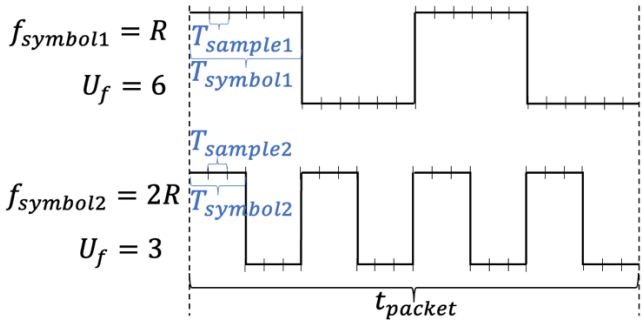


Figure 19. Schematic of data rate-adaptive technique.

The number of symbols in each packet is calculated as

$$N_{symbol} = \frac{N_{sample}}{U_f} = \frac{t_{packet}}{T_{sample} \times U_f}, \tag{26}$$

where N_{sample} is the total number of samples in each packet, T_{sample} is the sample period. The data rates can be calculated as

$$f_{symbol} = \frac{1}{T_{symbol}} = \frac{1}{T_{sample} \times U_f}. \tag{27}$$

According to (26) and (27), the up-sampling factor range, sample period T_{sample} and packet duration t_{packet} should be jointly decided, ensuring the resulting data rate range and data rate increment are rational for the proposed MIMO-VLC system.

The up-sampling factor range should be decided at first. The minimum value of the up-sampling factor should make sure the signal is over-sampled with a sampling rate above the Nyquist rate (which is twice the bandwidth of the signal). The maximum value of the up-sampling factor must not be too large but large enough to ensure there are enough options between the minimum and maximum values. After that, a reasonable data rate f_{symbol} range can be determined based on the up-sampling factor valued using (27). The data rate range should include the worse and best value that the actual data rate can achieve in the proposed system. Last, the number of symbols per packet N_{symbol} can be decided using (26) to ensure a rational

number of symbols in each data packet. Enough number of packets is also required. Both N_{symbol} and the number of packets ensure the simulation have the proper amount of transmitted data to get relatively accurate results within a reasonable simulation time.

2.5. Transmitter Coordination Algorithm

In section 1.4.1 of the literature review, spatial multiplexing (SMP), ganging, and spatial modulation (SM) have been introduced as common schemes used in MIMO-VLC systems. However, each of them has drawbacks under different channel conditions. Ganging only provides limited spectral efficiency as all LEDs are applied to transmit the same data sequence. SMP provides higher spectral efficiency than ganging, but its performance can be significantly decreased when there is spatial crosstalk. Here, a MIMO scheme combining ganging and SMP is introduced to improve the overall data rates over the receiver plane, referred to as the Channel Condition-based Transmitter Coordination (CCTC) algorithm. The CCTC algorithm coordinates transmitter patterns of LEDs to one or several group(s) and then optimises the overall data rates of each channel group. In the algorithm, when channels are well-conditioned, all channels can transmit different data sequences to achieve a high overall data rate as in SMP. However, when some channels have substantial spatial crosstalk between them for some receiver locations, the system will switch to an entirely or partially ganged scheme based on a given BER requirement to improve the overall performance.

Fig. 20 shows the CCTC patterns with different groupings of channels. If four channels are employed to transmit different data streams, there is one possible LED pattern, pattern 1. For pattern 2, there are six possible patterns, as three different data streams transmitted. For pattern 3, there are seven patterns with two independent channels. For pattern 4, there is only one pattern, and all channels transmit the same data stream.

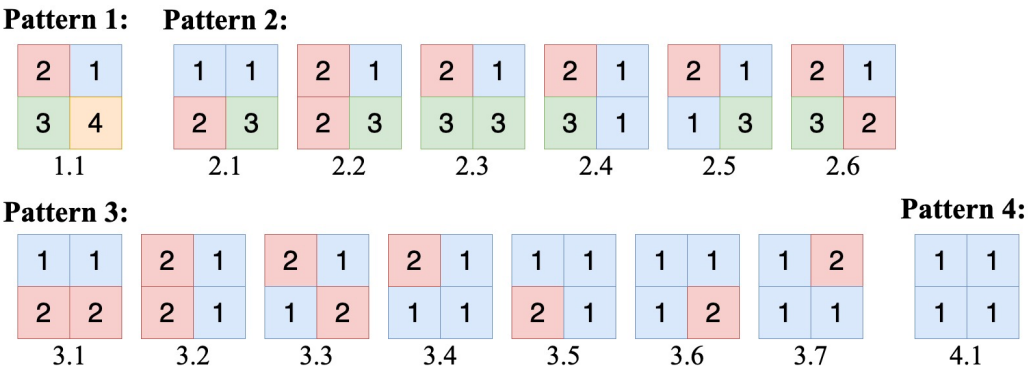


Figure 20. Channel condition-based transmitter coordination patterns.

At each user location, the BER for each transmission is monitored. The proposed algorithm decides whether to use a full ganging, SMP or the combination of SMP and ganging, depending on if the average BER is greater or smaller than 1×10^{-3}. Then it determines how high the data rates should be set for the selected pattern whilst meeting the BER requirement. This is achieved using DFE to equalise the channel when the data rate exceeds that which can be transmitted without distortion for the given channel bandwidth.

The transmitter operation is summarised in Algorithm 1.

Algorithm 1 Transmitter operation to achieve maximum data rate with BER $\leq 1 \times 10^{-3}$

1: Initialisation: Denote $\boldsymbol{U}_f$ as the vector temporarily stores the up-sampling factors of 1 to N_t LEDs, the number of channels is $c \leftarrow 4$ and pattern number is $pt^{(c)} \leftarrow 1$;

2: $\boldsymbol{d} = [0\ 0\ 0\ 0]$;

2: **while** $c >= 1$, **do**

3: At the specific receiver location (p_1, p_2), calculate $BER^{(c,pt)}$ of each channel and $BER_{overall}^{(c,pt)}$ average through channels;

4: **if** $BER_{overall}^{(c,pt)} \leq 1 \times 10^{-3}$ **then**

5: **if** $BER^{(c,pt)}$ of each channel $\leq 1 \times 10^{-3}$ while achieves the lowest $\boldsymbol{U}_f$ **then**

6: Store $\boldsymbol{U}_f$ and corresponding data rates $\boldsymbol{R_b}$ for receiver location (p_1, p_2):

7: **for** row = 1:c **do**

8: $\boldsymbol{U}(p_1, p_2, row) = \boldsymbol{U}_f(row)$;

9: $\boldsymbol{R}(p_1, p_2, row) = \boldsymbol{R_b}(row)$;

10: $\boldsymbol{R_{sum}}(p1, p2) = sum(\boldsymbol{R_b})$;

11: **end for**

12: **end if**

13: **for** row = 1:c **do**

14: **if** $BER^{(c,pt,row)} \leq 1 \times 10^{-3}$ **and** $\boldsymbol{U}_f \geq \boldsymbol{U}_l$ **and** $\boldsymbol{U}_f \leq \boldsymbol{U}_u$ **then**

15: $\boldsymbol{U}_f(row) = \boldsymbol{U}_f(row) - 1$;

16: $\boldsymbol{d}(row) = 1$;

17: **elseif** $BER^{(c,pt,row)} > 1 \times 10^{-3}$ **or** $\boldsymbol{U}_f < \boldsymbol{U}_l$ **then**

18: $\boldsymbol{U}_f(row) = \boldsymbol{U}_f(row) + 1$;

19: **elseif** $BER^{(c,pt,row)} > 1 \times 10^{-3}$ **and** $\boldsymbol{d}(row) == 0$

20: $\boldsymbol{U}_f(row) = \boldsymbol{U}_f(row) + 1$;

21: **end if**

22: **end for**

23: **elseif** $BER_{overall}^{(c,pt)} \geq 1 \times 10^{-3}$ **and** $c > 1$ **then**

24: $c \leftarrow c - 1$;

25: **elseif**

26: $\boldsymbol{U}(p_1, p_2) = NaN$;

27: $\boldsymbol{R_{sum}}(p1, p2) = NaN$;

28: **end if**

29: **end while**

In Algorithm 1, $\boldsymbol{U_f}$ is the vector that temporarily stores the values of the up-sampling factor with the lower and upper bound $\boldsymbol{U_l}$ and $\boldsymbol{U_u}$. $\boldsymbol{U}$ is the matrix that saves the final values of the up-sampling factors at each receiver position across the receiver plane. $\boldsymbol{R}$ is the matrix which saves the final data rates for all channels, $\boldsymbol{R_{sum}}$ is the matrix that saves the final overall data rate at each user location across the receiver plane.

The idea of the algorithm is, for each receiver location:

1. Test the overall BER for pattern 1 with each channel's initial up-sampling factor (with the corresponding initial data rate).
2. If overall BER $\leq 1\times10^{-3}$ for pattern 1, employ pattern 1 at this receiver location, otherwise skip to step 3.
   2.1. Examine the BER for each channel. Decrease the up-sampling factor by 1 (increase the data rate) if the channel BER $\leq 1\times10^{-3}$, until getting the highest data rates for each channel with channel BER $\leq 1\times10^{-3}$.
3. Swap from pattern 1 to pattern 2 and calculate the overall BER for pattern 2.1 to 2.6 in order. If any pattern achieves an overall BER $\leq 1\times10^{-3}$, repeat step 2.1 for these patterns and get the highest data rates for each channel. Otherwise, skip to step 4.
   3.1. Calculate the overall data rates for each chosen pattern and pick the pattern with the highest overall data rate.
4. If all patterns in pattern 2 have an overall BER $> 1\times10^{-3}$, repeat step 3 for pattern 3 and pattern 4 in order.
5. If the overall BER $> 1\times10^{-3}$ for pattern 4, increase the up-sampling factor (decrease the data rate) for each channel until the channel BER $\leq 1\times10^{-3}$.
6. If the channel BER $> 1\times10^{-3}$ when the up-sampling factor > 20 in pattern 4, output "NaN".

The BER is acquired by comparing the estimated bits and the transmitted bits. The reason for using BER ≤ 1×10^{-3} is because the value is below the forward error correction (FEC) limit 3.8×10^{-3} [60].

2.6. Performance Evaluation

2.6.1. Simulation Conditions

In this section, detailed simulation settings are introduced.

A. Transmitter

At the transmitter, up-sampling is applied before the LED sends the data. The generated data stream is extended to have U_f samples for each bit, creating a vector representing the time-domain waveform. The system settings of the simulation can be derived by substituting the parameter values into (26) and (27). With an up-sampling factor from 6 to 20, the corresponding numbers of symbols vary from 33333 to 10000, and the corresponding data rates per channel are from 100 Mbps to 333.33Mbps, which is a sufficiently large range. The data rate of each channel is individually optimised, which helps the system achieve the highest overall data rates.

The transmission time of each packet t_{packet} is set to 0.1 ms, and the sample duration T_{sample} is set to 0.5 ns. Hence there are 200 thousand samples per channel per packet using (26). In total, 50 packets are transmitted, over which the obtained values of BER are averaged. Perfect knowledge of the channel matrix is assumed.

B. Receiver

At the receiver side, the DFE and down-sampling are employed after the matrix decoupling. In the simulation, the DFE uses 24 feedforward and 19 feedback filter taps. Section 2.3.2

investigates the DFE mechanisms and the relation among the step size, training length, and system settings. The step size adapted for this system is 0.01.

The training length is 200 thousand samples for each receiver location. This corresponds to bit lengths from10000 to 33333, depending on the up-sampling factor. This is much greater than the 2000 bits required for the SISO system in section 2.3.2. The reasons are as follows: First, each channel in the MIMO system is affected by the crosstalk from other channels due to the noise and the imperfect deconvolution, making the DFE equalisation more difficult. Second, the MIMO system can have a much higher data rate (200 Mbps) per channel than the SISO one (120 Mbps), and a higher data rate requires a longer training length.

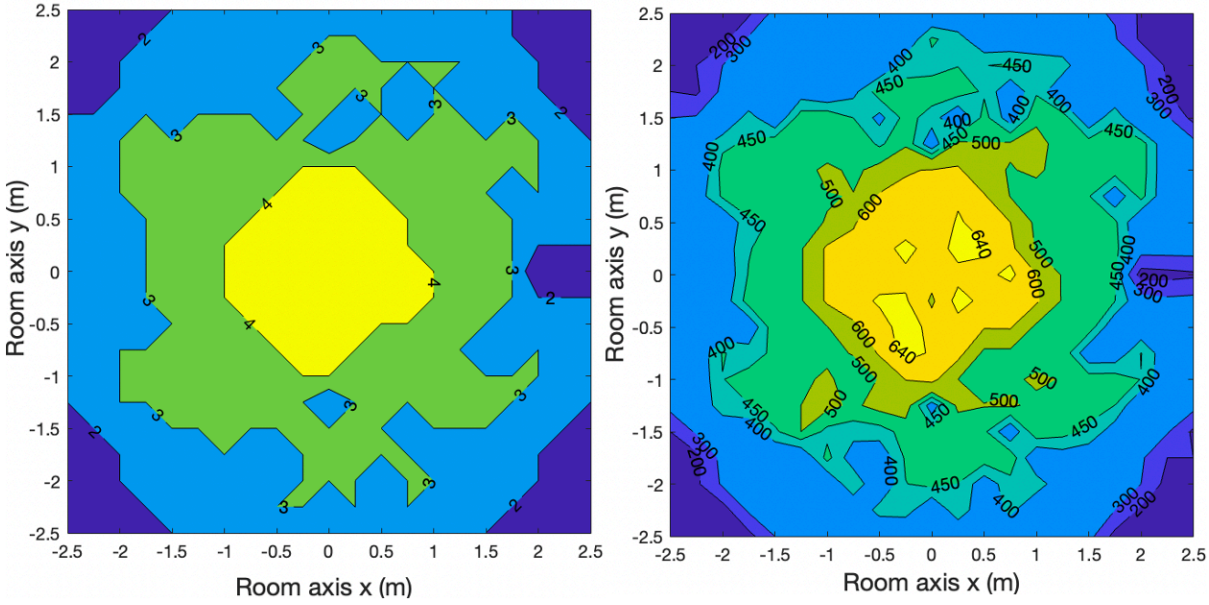
After the training process is complete, the weighting coefficients of the DFEs are fixed, and the well-trained DFEs can then be employed to process the actual data. Each channel, or group of channels, has a separate equaliser. The DFEs are retrained using a training sequence with 200 thousand samples whenever the receiver changes its position in the room.

Then, maximum likelihood (ML) detection is applied to estimate the received bits, obtaining the estimation of the transmitted binary bits from each source. The BER is obtained by comparing the estimated bits and the transmitted bits. Then the overall data rates are calculated using Algorithm 1.

2.6.2. Performance Comparison with Seven-Channel ADR System

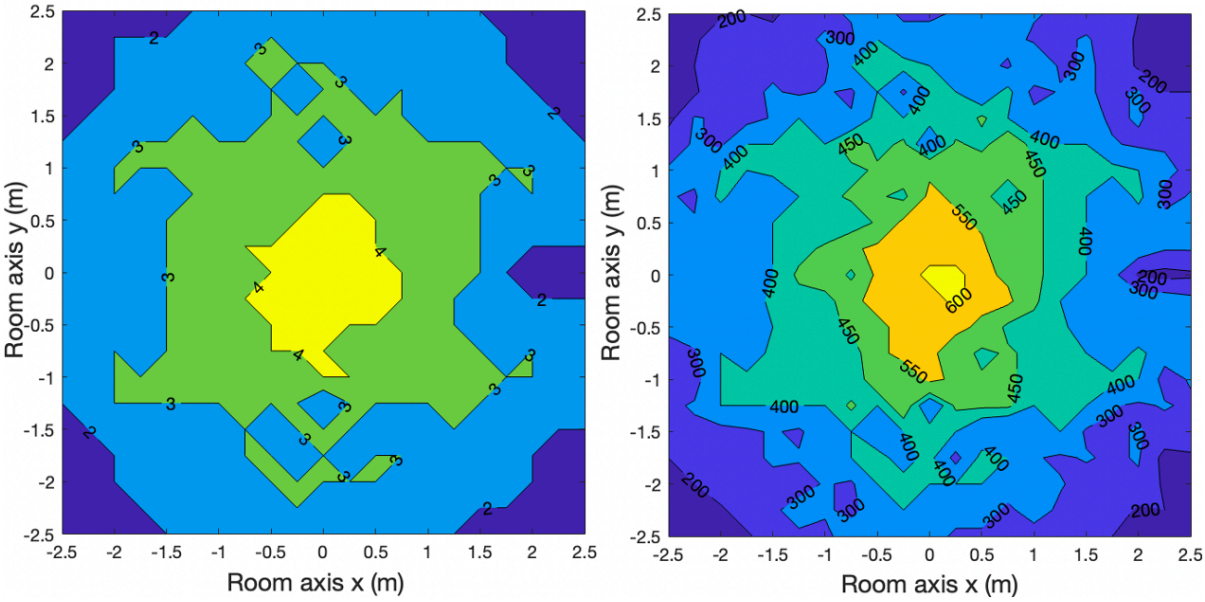
The VLC system with seven-channel ADR implemented is first investigated. Fig. 21 shows the number of channels and the overall data rate distribution across the receiver plane of the proposed system with the adaptive data rate and Algorithm 1. This system is referred to as case A. Fig. 22 presents the number of channels and the overall data rate distribution of the system without an adaptive data rate and with Algorithm 1. This case is referred to as case B. The overall data rate distribution of an SMP system with a non-adaptive data rate is shown in Fig.

23. In this case, four channels are used across the room. This system is considered as case C. In these figures, the overall data rates increase progressively from the edge of the room to its centre. The figures are expected to be perfectly symmetrical around the x-axis and y-axis, given the system geometry. However, in practice, the asymmetry occurs due to the limited resolution of the simulation and a limited number of transmitted packets.



(a) (b)

Figure 21. Case A: Seven-channel ADR system with adaptive data rate and with Algorithm 1. (a) Distribution of number of channels (b) Distribution of overall data rate (Mbps).



(a) (b)

Figure 22. Case B: Seven-channel ADR system without adaptive data rate and with Algorithm 1. (a) Distribution of number of channels (b) Distribution of overall data rate (Mbps).

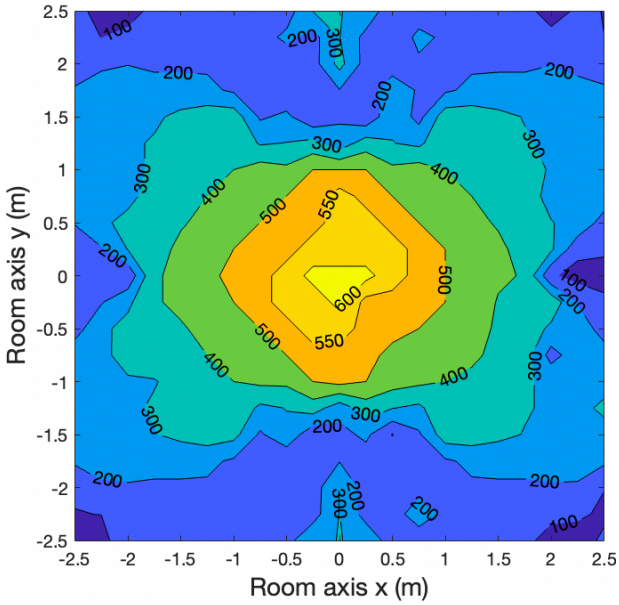


Figure 23. Case C: Overall data rate (Mbps) distribution of the seven-channel ADR system without adaptive data rate and with conventional SMP.

The mean aggregate data rate versus receiver distance to the room centre is plotted in Fig. 24 based on Fig. 21(b), Fig. 22(b), and Fig. 23. Each marked point on the plot is the mean of the data ±0.25m on either side of the distance from the room centre. First, the performance of cases B and C are compared. Fig. 24 shows that the overall data rate significantly decreases from the middle to the edge in case C. This results from the system's increased matrix condition number and the decreased signal-to-interference-plus-noise ratio (SINR). In case B, the impact of the ill-conditioned channel matrix is mitigated by employing partial ganging. The channels with higher interference and lower SINR are combined to transmit the same data sequence, which significantly improves the data rates of the poor channels. The system in case B shows a significant data rate improvement compared with case C except for the area in the room centre because all four channels have good quality here, and pure SMP is used in both cases in this area. The overall data rate improves by 22 per cent on average in case B compared with case C.

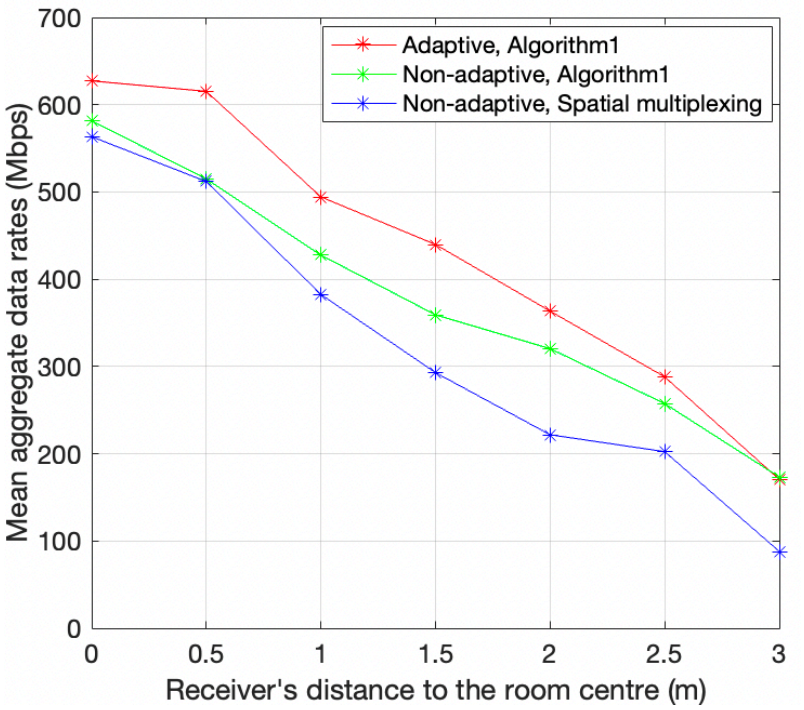
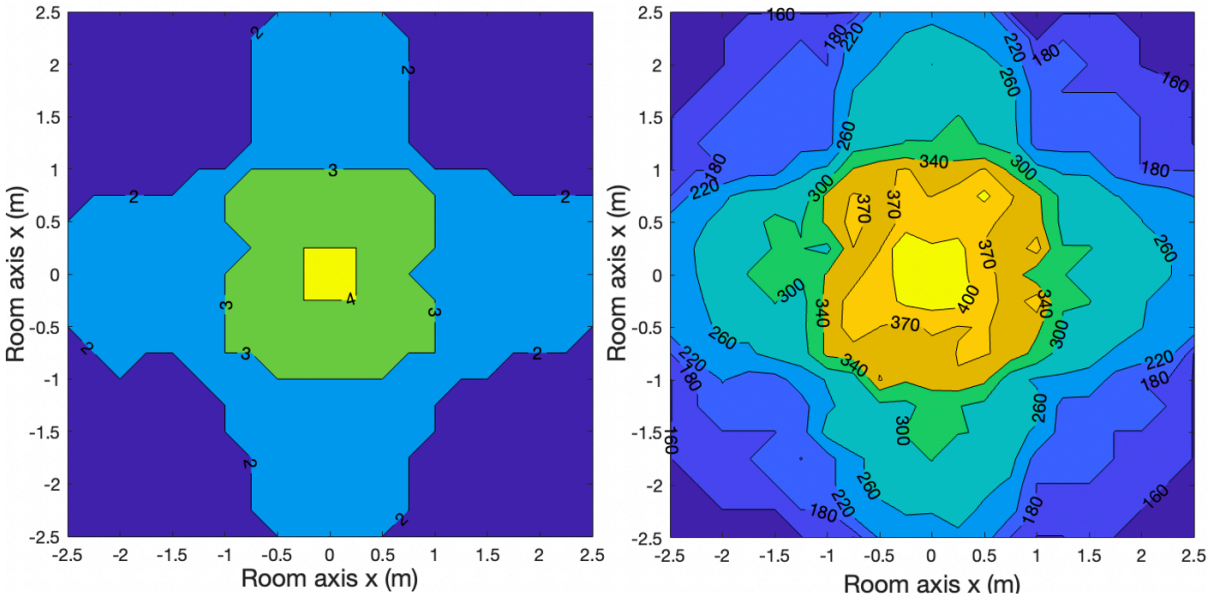


Figure 24. Mean aggregate data rates versus the receiver's distance to the room centre.

The data rate performance further increases when data rate-adaptive modulation is applied in case A. The peak overall data rate in Fig. 21(b) is 676 Mbps. The average overall data rate in case A is 15 per cent higher than that in case B. This is because even though the poor channels are combined in case B, the same data rate (up-sampling factor) is still used by all channel groups, and it is not optimised based on the different channel conditions of the group. In case B, the channel groups with high SINR must conform to those with lower SINR and cannot reach their optimal data rate. The data rate improvement also vanishes at the four corners of the room because pure ganging is applied here in both case A and case B, and there is only one channel group. In summary, the overall data rate is improved by 41 per cent (on average across the room) in case A compared with case C.

2.6.3. Performance Comparison with Aperture-Based Receiver System

Work in this section analyses the performance of the proposed adaptive system with an ABR installed. Fig. 25 presents the number of channels and the overall data rate distribution of the proposed system employing data rate-adaptive modulation and Algorithm 1. The overall data rate distribution of an SMP system with a non-adaptive data rate is presented in Fig. 26. The peak overall data rate is 434 Mbps in Fig. 25. The proposed techniques improve the overall data rate of the system in Fig. 25 by 127 per cent on average, compared with that in Fig. 26.



(a) (b)

Figure 25. ABR system with adaptive data rate and with Algorithm 1. (a) Distribution of number of channels (b) Distribution of overall data rate (Mbps).

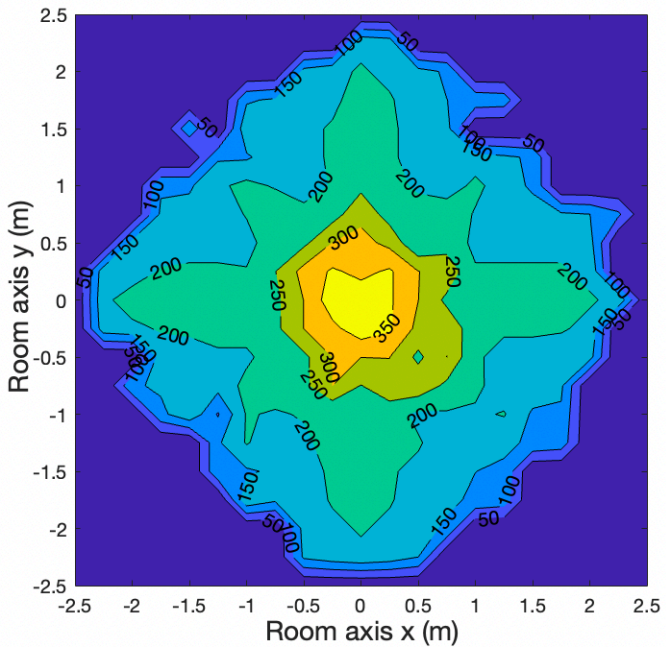


Figure 26. Overall data rate (Mbps) distribution of the ABR system with non-adaptive data rate and SMP.

ADR and ABR are also compared in the new adaptive system. The highest overall data rate of the ADR-based system (676 Mbps) is 56 per cent higher than the data rates of the ABR-

based system (434 Mbps). The average overall data rate of the ADR-based system (406 Mbps) is also 64 per cent higher than that of the ABR-based system (247 Mbps). This difference is mainly caused by the different sizes of the detection area. To guarantee that two types of receivers possess a similar size, the collection area of each RE in the seven-channel ADR is set the same as the detection area of each RE in the ABR. However, the usable detection area of each RE in the ABR is much smaller than that of each RE in the seven-channel ADR because a large portion of the light spot area is blocked by the opaque screens in the ABR system. Even though the ABR has eight REs, its overall detection area is still smaller than that of the ADR with seven REs. In addition, the full angle FOV of the ABR is larger than that of the seven-channel ADR by around 30° because it does not have a concentrator. This means more ambient noise is assumed to be detected by the ABR in the simulation.

2.6.4. Conclusions

A CCTC algorithm and a data rate-adaptive modulation are proposed in a typical indoor MIMO-VLC system to improve the communication speed of the system. Two types of angular diversity receivers: a seven-channel ADR and an ABR, are implemented.

The proposed scheme is compared with the conventional SMP scheme. The proposed channel adaptive system effectively mitigates spatial crosstalk and temporal crosstalk. It outperforms the conventional SMP system with 41 per cent improvement with the ADR and 127 per cent improvement with the ABR. Two angular diversity receivers are also compared in the new adaptive system. The peak overall data rate of the ADR-based system is 56 per cent higher than the data rates of the ABR-based system. The average overall data rate of the ADR-based system is also 64 per cent higher than that of the ABR-based system. Hence, the proposed ADR is supposed to provide better performance than the ABR.

Although the CCTC algorithm offers significant performance improvement to the system, it takes a large amount of computing time as it employs an exhaustive search to find the optimal patterns and data rates. A solution to reduce the computational complexity of the CCTC algorithm is required, which is explored in Chapter III. The ADR-based system is expected to offer higher data rate performance than the ABR-based system. Therefore, the ADR-based system is employed in further studies.

CHAPTER III: NEURAL NETWORK-BASED MIMO-VLC SYSTEM

In Chapter II, the CCTC algorithm was proposed to improve the overall data rate of the MIMO system. However, this algorithm requires a large amount of computing time as it optimises the patterns and the data rates across the room by iterating through all the possible options, as shown in Algorithm 1. Hence, a solution with smaller computational complexity is needed, and this is explored in this chapter.

3.1. Introduction

Artificial neural networks (ANN) are a set of computing systems that roughly simulate how the human brains analyse information [61]. They can learn patterns through detecting relationships in data [62], which means they can also save computing time by predicting the result using the learned relationships. Fig. 27 shows a typical feedforward multi-layer perceptron (MLP) structure ANN. The neural network is composed of one input layer, one or multiple hidden layer(s) and one output layer. Tens or hundreds of artificial neurons are organised in each layer. The initial output of each neuron is calculated as the input values from the former layer times their weights. These weighted inputs are added together, and then the neuron adds a bias b [62]. As an example, if there are three neurons in the input layer, the initial output of the neuron y_0 in Fig. 27 is calculated as

$$y_0 = \boldsymbol{x} \cdot \boldsymbol{w} + b_0 \,, \tag{28}$$

where $\boldsymbol{x} = [x_0\ x_1\ x_2]$ is the input vector of the neuron, $\boldsymbol{w} = [w_{0,0}\ w_{1,0}\ w_{2,0}]^T$ is the weight vector and b_0 is the bias of y_0.

Except for the nodes at the input layer, every node has a non-linear activation function (transfer function). The neuron's output is obtained after passing the sum of the weighted inputs (with bias) through the activation function [62].

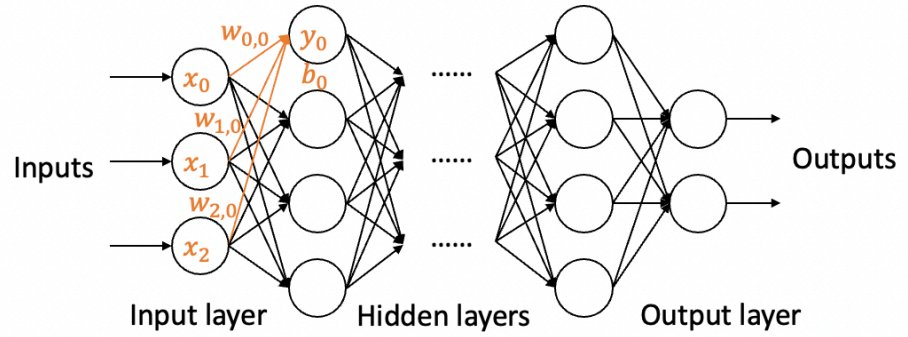


Figure 27. Multi-layer perceptron neural network structure.

ANNs are widely used in a variety of science fields. They have also been employed in indoor VLC systems. A mobile user positioning system based on trilateration estimation and ANN estimation are described in [63]. Reference [64] demonstrates a neural network-based 3D positioning system with high precision (resolution of < 1cm). Works reported in [65], [66], [67], and [68] explore the ANN-based physical layer techniques in the VLC systems. Reference [65] introduces a neural decoding model which bundles the decoding abilities of a square wave quadrature amplitude modulation (SW-QAM) to undertake light source localisation and interference estimation. Reference [66] employs a convolutional neural network (CNN) to build a demodulator, identifying the signals through image classification. Recurrent neural networks (RNNs) are used in [67] to design a deep learning-based run-length limited (RLL) decoder with reduced computational complexity compared with the conventional RLL decoding scheme. Reference [68] presents an ANN-based joint equaliser system that combines spatial and temporal equalisation to compensate for the crosstalk and improve the achievable data rate. As shown in these previous VLC-related works, ANNs can either reduce the

computational complexity of the system or improve the system performance. To the best of the author's knowledge, there is no work applying a neural network to predict the transmitter patterns and data rates. The employment of the neural network to replace the CCTC algorithm is expected to decrease the computational complexity of the system described in Chapter II.

In the following sections, the ANN technique will be employed in the proposed MIMO-VLC system to replace the CCTC algorithm and find the optimal transmitter pattern with reduced computing time.

3.2. Pattern Coordination with Neural Network

The Feedforward MLP ANN is a commonly used network that can work with a variety of problems such as non-linear prediction and pattern recognition. In this work, it is employed to replace the CCTC algorithm and predict the optimal transmitter pattern. There are two stages in the CCTC algorithm, as mentioned in section 2.5:

(1) Select the optimal transmitter pattern by coordinating channels into one or several channel group(s).

(2) Determine the optimal up-sampling factor (data rate) for each ganging group.

In this section, the MLP ANN estimates the optimal transmitter pattern at each user location and replaces stage (1) of the CCTC algorithm. Fig. 28 shows the architecture of the network. The system is a two-layer feedforward network, including one input layer, which uses the channel matrix as inputs, one hidden layer and one output layer, which outputs the optimal pattern index. After obtaining this, each channel group's up-sampling factor (and therefore the data rate) is maximised by the CCTC algorithm in stage (2). The requirement BER $\leq 1\times10^{-3}$ is employed in this chapter, the same as the BER requirement used in Chapter II.

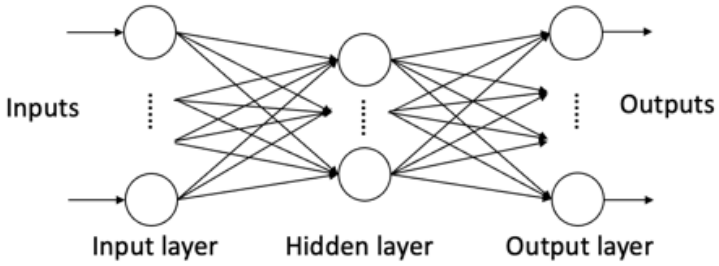


Figure 28. Architecture of the MLP ANN.

The selection of the optimal transmitter pattern is a pattern recognition problem, which means the neural network can identify the corresponding target category for each input. The MIMO channel matrix between the transmitter and the receiver is introduced in (4) in section 2.1.2. There are $N_r \times N_t$ weights in the channel matrix, and the number of neurons at the input layer is set to this number. The input layer is connected with the hidden layer, and the hidden layer uses the sigmoid function as the activation function. The output layer has a softmax function. The number of neurons at the output equals the number of different transmitter patterns. The output performance is evaluated by calculating the cross-entropy between the results obtained from the CCTC algorithm and that predicted by the MLP ANN.

A Small cross-entropy value indicates that the desired output value and the actual output value of the neural network is close to each other. Cross-entropy is used to judge the quality of the weights and biases of the neural network and direct the adjustment of them. Fig. 29 presents a network diagram with a backpropagation learning rule to update the weights and biases. The weights and biases are optimised using a gradient descent technique to reach the minimum value of the cross-entropy [61]. After obtaining the optimal weights and biases, the neural network is regarded as well-trained and can be employed to predict the transmitter pattern of the MIMO-VLC system. Once the transmitter pattern is known, the performance of each of the data streams is optimised using Decision Feedback Equalised (DFE) On-Off-Keying (OOK)

as a modulation scheme. Other parameters can be found in Table I in section 2.1, and other system settings are the same as the system model in section 2.1.

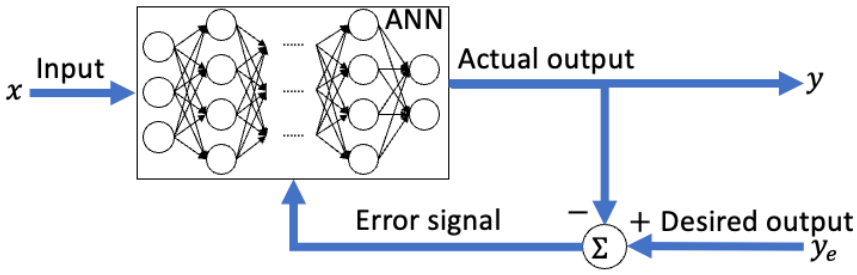


Figure 29. Network diagram with backpropagation learning rule.

3.3. Initial Tests

First, the neural network is employed to predict the optimal transmitter pattern with varying receiver positions relative to the LEDs, even with the receiver location out of the range in the training data. The neural network-based system is tested with different room sizes.

3.3.1. System Settings

On the input side, the number of neurons is $N_r \times N_t = 28$. The hidden layer has 10 neurons. The number of neurons at the output side is 15 as there are 15 transmitter patterns, as shown in Fig. 20. The MLP ANN system has two phases: a training phase and a testing phase. In the training phase, rooms with 7m × 7m × 3m (Room T_1) and 7m × 7m × 4.5m (Room T_2) are selected. 225 channel matrices obtained from 225 (15 × 15) different user locations (picked from the receiver plane with a 0.5m array pitch) are employed for each testing room. In total, 450 channel matrices form the inputs, and the corresponding 450 patterns calculated from the CCTC algorithm are used as the targets.

In the testing phase, three different room sizes are employed, as shown in Table III. Room A has the same height as Room T_1. Room B has a higher height than the rooms used in the

training phase. Room C has a shorter height but larger coverage area than the rooms used in the training phase.

Table III. Room types in testing phase

Room type	**Room size (width × length × height)**	**Testing points**	**Array pitch**
A	4.5m × 4.5m × 3m	10 × 10 = 100	0.5m
B	6m × 6m × 5m	7 × 7 = 49	1m
C	8m × 8m × 2m	9 × 9 = 81	1m

The results obtained from the MLP ANN are compared with the results obtained from the CCTC algorithm. In addition, if the patterns derived from the MLP ANN cannot meet the BER requirement at some locations, the patterns are directly changed to ganging at these locations.

Fig. 30 shows the mean aggregate data rates versus distance from the receiver to the room centre for room A. Each marked point on the plot is the mean of the data ±0.25m on either side of the distance from the room centre. The height of room A is equal to the height of the training room (Room T_1). Each testing point is set at the centroid of every four adjacent training points in Room T_1. Fig. 30 presents that the mean aggregate data rates across the room derived from MLP ANN and CCTC algorithm are in good agreement.

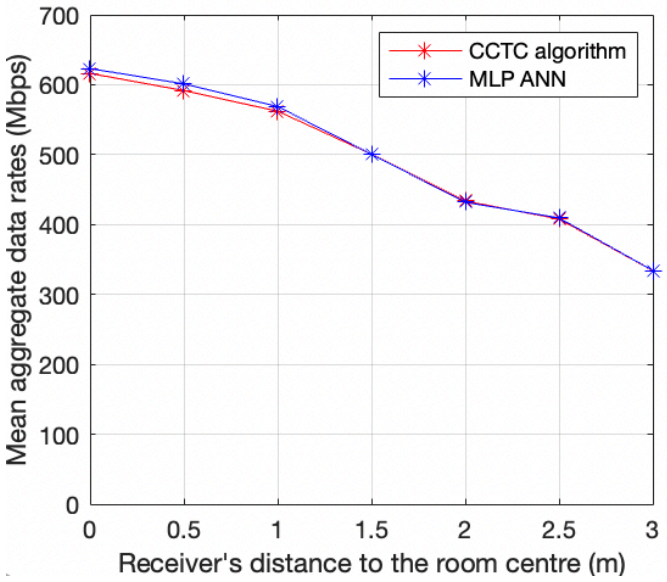


Figure 30. Room A: Mean aggregate data rates versus receiver's distance to the room centre.

Fig. 31 presents the mean aggregate data rates versus distance from the receiver to the room centre for room B. The height of room B is taller than that of the training rooms. Thte mean aggregate data rates across the room derived from MLP ANN and the CCTC algorithm closely resemble each other. The results of room B confirm that the MLP ANN can predict the optimum transmitter pattern, even though the room is taller than the rooms used to train the MLP ANN.

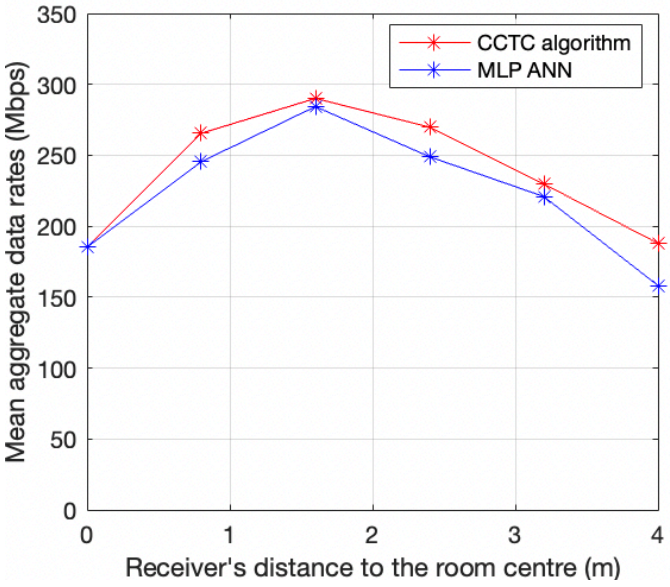


Figure 31. Room B: Mean aggregate data rates versus receiver's distance to the room centre.

Fig. 32 presents the mean aggregate data rates versus distance from the receiver to the room centre for room C. Room C has a lower room height than the room heights used in the training phase. However, it has a larger coverage area outside the coverage of training sets. This means that room C also reaches larger irradiance angles (from the LEDs to user locations at or near the room corners) than the rooms used in the training phase. Fig. 32 shows similar mean aggregate data rates across the room derived from the MLP ANN and the CCTC algorithm.

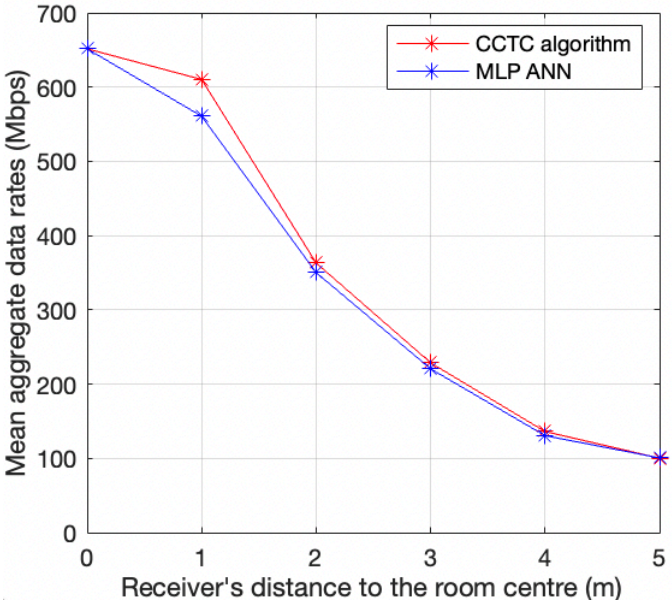


Figure 32. Room C: Mean aggregate data rates versus distance to the room centre.

The results above confirm that the MLP ANN can predict the optimum transmitter pattern and achieve the highest data rate across the room, even changing the room height and the coverage area.

The computing time using both the MLP ANN and CCTC algorithm is presented in Table. IV below. The MLP ANN is around a factor of three faster than the CCTC algorithm. The computing time is obtained using MATLAB R2020b with an Intel i7-9700 eight-cores CPU.

Table IV. Computing time for MLP ANN and CCTC algorithm

Room type	**Room size (width × length × height)**	**MLP ANN computing time**	**CCTC algorithm computing time**
A	4.5m × 4.5m × 3m	4.08h	17.67h
B	6m × 6m × 5m	1.25h	5.51h
C	8m × 8m × 2m	1.63h	10.17h

3.4. Orientation Changes of the Receiver

Work in previous sections shows that the ANN performs well, even when the testing data falls outside the scope of the training data. So far, the modelling has considered translation of the receiver in the 3D room space. In this section, the rotation of the receiver relative to the transmitters is considered.

Fig. 13 in section 2.1.4 shows that the top view of the seven-channel ADR is a hexagon, which has six rotational symmetries, occurring every 60 degrees. Hence, only receiver rotation from 0 to 60 degrees needs to be considered in this section.

3.4.1. Receiver Yaw Rotation

At first, the receiver yaw rotation is investigated. Fig. 33 presents the receiver in the coordinate system. The receiver can rotate about the z-axis. The yaw rotation angle ψ is between the projection of the RE1's pointing direction on the xy-plane and the x-axis's positive direction.

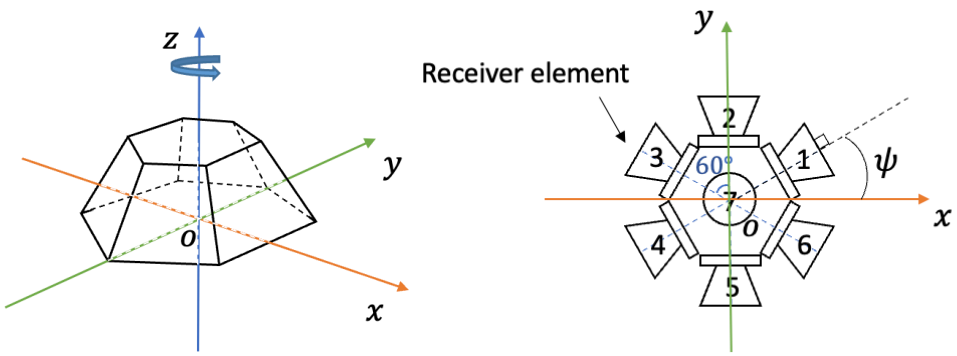


Figure 33. Receiver yaw rotation: (a) receiver rotation about z axis in the coordinate system, (b) top view of the receiver with yaw angle ψ.

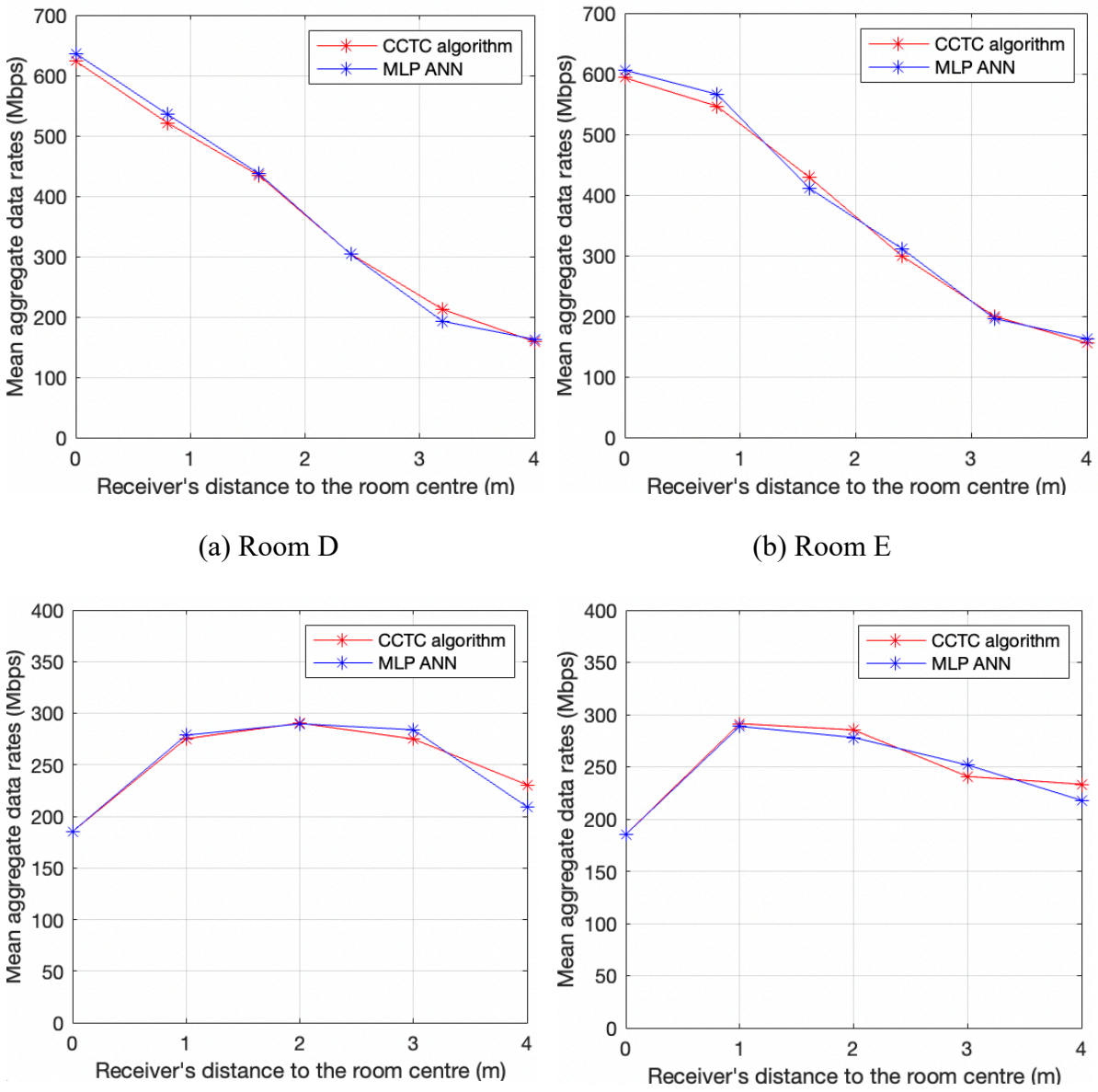
The training data is obtained from room sizes of 7m × 7m × 3m with yaw angle $\psi = 30°$ and 7m × 7m × 4.5m with $\psi = 30°, 60°, 75°$. The array pitch for each of the data sets is 0.5m.

In the testing phase, four types of rooms are employed, as shown in Table V.

Table V. Room types in testing phase

Room type	**Room size (width × length × height)**	**Yaw angle (ψ)**	**Testing points**	**Array pitch**
D	6m × 6m × 3m	45°	7 × 7 = 49	1m
E	6m × 6m × 3m	67.5°	7 × 7 = 49	1m
F	6m × 6m × 5m	45°	7 × 7 = 49	1m
G	6m × 6m × 5m	67.5°	7 × 7 = 49	1m

The mean aggregate data rates derived from MLP ANN and CCTC algorithm are in good agreement, as shown in Fig. 34(a)-(d). The results show that the MLP ANN can successfully predict the transmitter pattern, even changing the yaw rotation degree and the room height.



(a) Room D

(b) Room E

(c) Room F

(d) Room G

Figure 34. Mean aggregate data rate versus distance to the room centre.

The computing time obtained from MLP ANN and the CCTC algorithm are presented in Table VI. The MLP ANN is a factor of four to five times faster than the CCTC algorithm.

Table VI. Computing time for MLP ANN and CCTC algorithm

Room type	**Room size (width × length × height)**	**Yaw angle (ψ)**	**MLP ANN computing time**	**CCTC algorithm computing time**
D	6m × 6m × 3m	45°	1.60h	7.92h
E	6m × 6m × 3m	67.5°	1.74h	7.86h
F	6m × 6m × 5m	45°	1.76h	6.91h
G	6m × 6m × 5m	67.5°	1.50h	6.01h

3.4.2. Receiver Roll Rotation

This section investigates the effect of receiver roll rotation with the geometry given in Fig. 35. The receiver can rotate about the y-axis. The roll angle ϕ is the angle between the bottom surface of the receiver and the positive direction of the x-axis.

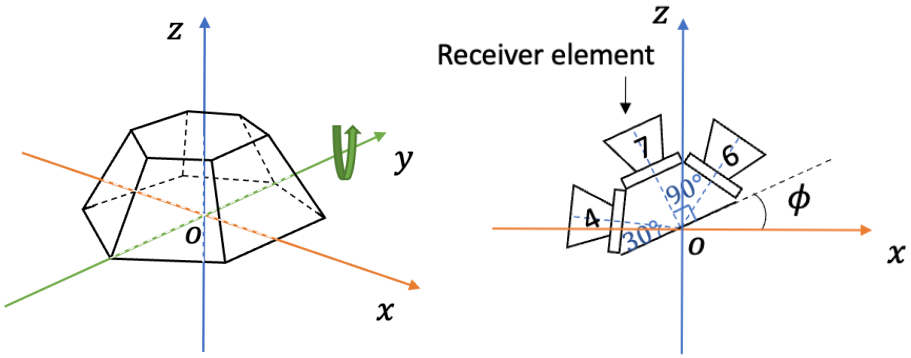


Figure 35. Receiver roll rotation: (a) receiver rotation about y axis in the coordinate system, (b) front top view of the receiver with roll angle ϕ.

The training data is obtained from:

(1) Room size of 6m × 6m × 3m with $\psi = 0°$ and $\phi = 0°$ and with $\psi = 0°$ and $\phi = 30°$, array pitch = 0.5m.

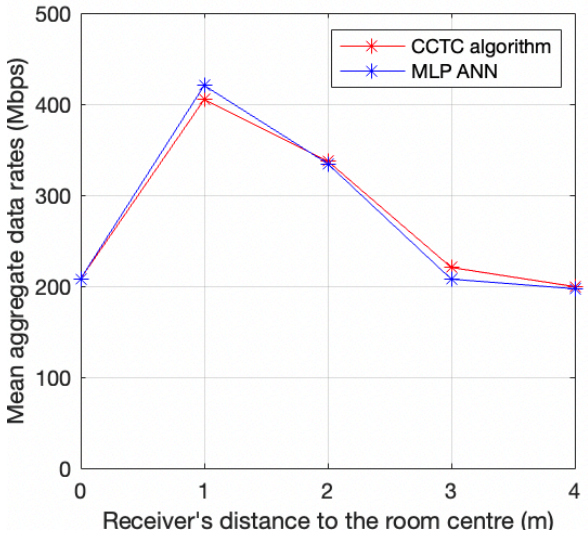
(2) Room size of 6m × 6m × 4.5m with $\psi = 0°$ and $\phi = 0°$ and with $\psi = 0°$ and $\phi = 30°$, array pitch = 0.5m.

Table VII gives the settings of three types of rooms employed in the testing phase.

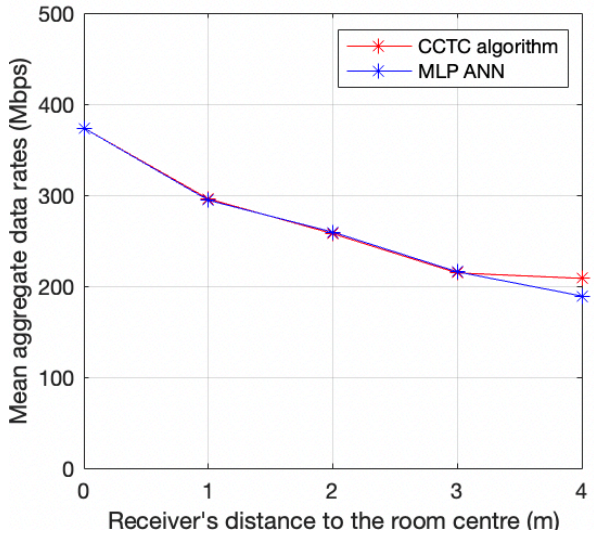
Table VII. Room types in testing phase

Room type	**Room size (width × length × height)**	**Yaw angle (ψ)**	**Roll angle (ϕ)**	**Testing points**	**Array pitch**
H	6m × 6m × 3m	0°	40°	7 × 7 = 49	1m
I	6m × 6m × 5m	0°	20°	7 × 7 = 49	1m
J	6m × 6m × 2m	0°	20°	7 × 7 = 49	1m

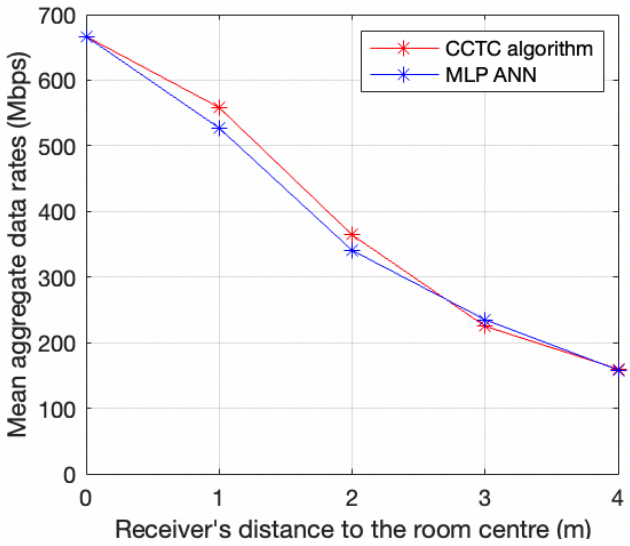
The mean aggregate data rates obtained from the MLP ANN and the CCTC algorithm can be found in Fig. 36. The results are in good agreement, which means that the neural network can efficiently obtain the optimal pattern, even changing the room height and the roll rotation angle. Fig. 36(a) also presents that the neural network works well even if the incident angles of some REs (at the room corner) fall outside the scope of the training data.



(a) Room H



(b) Room I



(c) Room J

Figure 36. Mean aggregate data rate versus distance to the room centre.

The computing time obtained from the MLP ANN and the CCTC algorithm is shown in Table VIII. The system using MLP ANN only spends around one-third of the CCTC algorithm's computing time.

Table VIII. Computing time for MLP ANN and CCTC algorithm

Room type	**Room size (width × length × height)**	**Roll angle (ϕ)**	**MLP ANN computing time**	**CCTC algorithm computing time**
H	6m × 6m × 3m	40°	1.85h	4.49h
I	6m × 6m × 5m	20°	1.35h	5.06h
J	6m × 6m × 2m	20°	2.22h	6.23h

3.5. Receiver with Human Walking Activity Model

Work in previous sections shows that the MLP ANN can predict the optimal transmitter pattern for receiver roll and yaw rotation as well as receiver translation. In this section, a model of receiver orientation and location for a typical mobile device user is incorporated into the algorithm testing. This model creates a series of coordinates and orientations for a typical mobile device user walking through a space.

3.5.1. Receiver Orientation Model

In [69], an experiment was conducted (with 40 participants and 222 datasets) to develop a statistical model of the mobile device's orientation while the user is using it. This reference introduces an orientation-based random waypoint (ORWP) mobility model, which shows the random orientation and position of the receiver during the walking activities of the user. The ORWP model is employed in this section to test the performance of the neural network.

The schematic of the mobile device with the inbuilt receiver is shown in Fig. 37. The schematic exhibits the pointing direction of each RE relative to the mobile device.

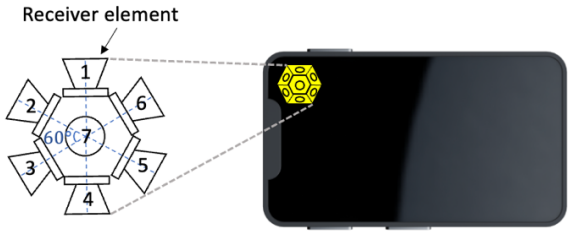


Figure 37. Mobile device with the seven-channel ADR installed (receiver size not to scale).

Two coordinate systems are introduced to represent the orientation of the mobile device. The mobile device local coordinate system is defined with xyz, and the geographic coordinate system is presented with XYZ, as shown in Fig. 38(a) [69]. Fig. 38 shows the rotation of the mobile device around the x, y and z axes. The rotation angles are called yaw angle (ϕ_1), pitch angle (ϕ_2) and roll angle (ϕ_3) as shown in Fig. 38(b)-(d), respectively.

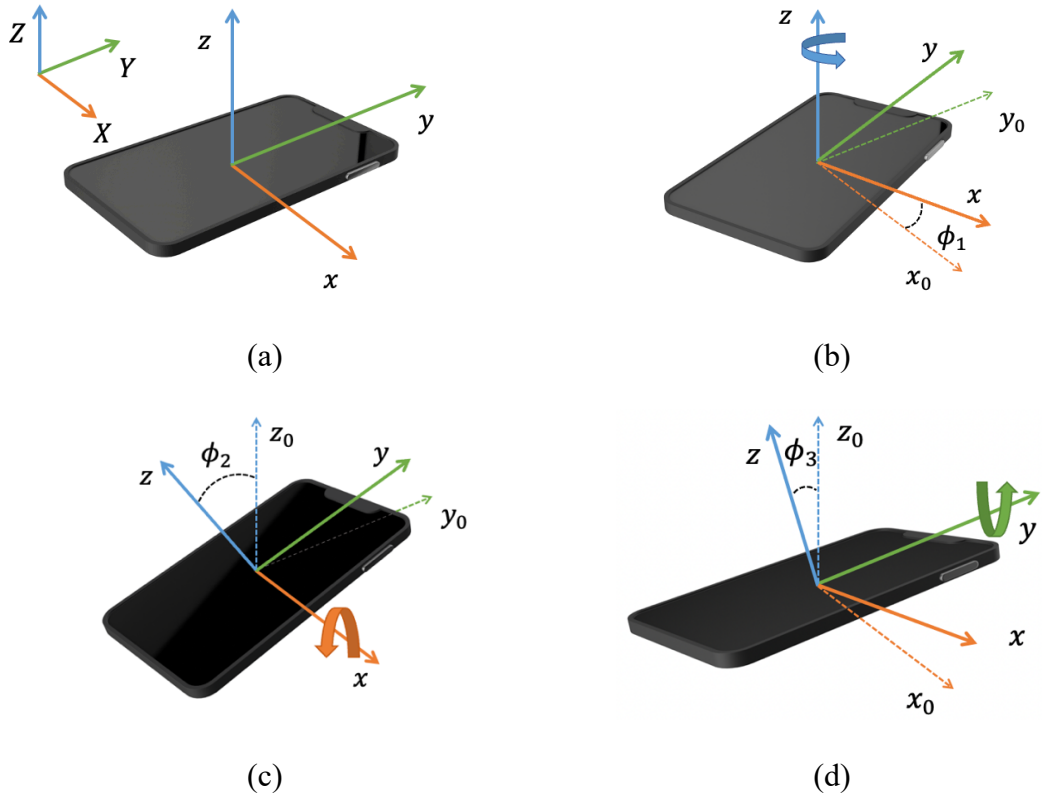


Figure 38. Orientation of the device: (a) original orientation, (b) yaw rotation around z-aixs, with angle ϕ_1, (c) roll rotation around y-axis, with angle ϕ_2, (d) pitch rotation around x-axis, with angle ϕ_3 [69].

The normal vector of the xy-plane of the mobile device is set as $\boldsymbol{n} = [n_1, n_2, n_3]^T$. The original direction is assumed as $\boldsymbol{n} = [0,0,1]^T$. $\boldsymbol{n}$ is in a cartesian coordinate system can be transferred to the spherical coordinate system, which can be expressed in polar angle θ and azimuth angle φ.

The polar angle θ is the angle between the normal vector $\boldsymbol{n}$ and the positive direction of the Z-axis, which is calculated in [69] as

$$\theta = cos^{-1}(cos\phi_2 cos\phi_3)\,. \tag{29}$$

The azimuth angle φ is the angle between the projection of $\boldsymbol{n}$ on the XY-plane and the positive direction of the X-axis, which is obtained as

$$\varphi = tan^{-1}\left(\frac{sin\phi_1 sin\phi_3 - cos\phi_1 cos\phi_3 sin\phi_2}{cos\phi_3 sin\phi_1 sin\phi_2 + cos\phi_1 sin\phi_3}\right). \tag{30}$$

The experiment in [69] presents that the probability density function (PDF) of the azimuth angle φ shows a nearly uniform distribution $\varphi \sim \mathcal{U}[-\pi, \pi)$. The PDF of the polar angle θ follows the Gaussian distribution $\mathcal{N}(\mu, \sigma^2)$ with mean $\mu = 29.67°$ and standard deviation $\sigma = 7.78°$.

3.5.2. Orientation Random Waypoint Model of the Receiver

As mentioned before, the ORWP model [69] is employed to describe the receiver orientation and user mobility. In the model, users can walk into the room with the mobile device held at the height of the receiver plan. Users pick the destination randomly within the indoor area and walk in a straight line from the start to the destination with a constant walking speed. There are lots of waypoints during two adjacent destinations, and each of them has different orientations. In our model, the device is only used in landscape mode (heading to the positive direction of the x-axis in the mobile device local coordinate system).

In each movement, the user moves from the random waypoint $P_{n-1} = (x_{n-1}, y_{n-1})$ to $P_n = (x_n, y_n)$ with $n \in \mathbb{N}$. The distance between two successive waypoints P_n and P_{n-1} is the transition length $\mathcal{L}_n$. The transition lengths $\{\mathcal{L}_1, \mathcal{L}_2, \mathcal{L}_3 \ldots\}$ are independent identically distributed (i.i.d.) random variables (RVs). The PDF of the RVs is shown in [70]. In a $L \times L$ (width × length) squared room, the expected length of the RVs is $\mathbb{E}[\mathcal{L}] = 0.5214L$.

The polar angle θ is modelled as a correlated Gaussian random process [69]. The nth time sample of the correlated Gaussian random process is

$$\theta[n] = c_0 + c_1\theta[n-1] + \omega[n], \tag{31}$$

where $\omega[n]$ is the nth time sample of the white noise process and with

$$c_0 = (1 - c_1)\mathbb{E}[\theta], \tag{32}$$

$$\sigma_\omega^2 = (1 - c_1^2)\sigma_\theta^2, \tag{33}$$

$$c_1 = 0.05^{\frac{T_s}{T_{c,\theta}}}, \tag{34}$$

where $T_{c,\theta}$ is the coherence time of the polar angle, T_s is the sampling time and σ_ω^2 is the variance of ω.

The parameters used in the modelling are shown in Table IX. The receiver plane height is revised from 0.85m to 1m to ensure the vertical distance between the transmitter and the receiver is 2m, the same as the setting in [69]. Other system settings can be found in Table I in section 2.1.

Table IX. Parameters

Parameters	Values
Room size (width × length × height)	6m × 6m × 3m
Receiver plane height	1m
Coherence time of the polar angle [71]	130ms
Sampling time (T_s) [69]	13ms
User walking speed [69]	2m/s

3.5.3. Water-Filling Algorithm

In order to benchmark the CCTC algorithm and the MLP ANN against other approaches, a MIMO approach that uses water-filling is also simulated. The water-filling algorithm can achieve optimal power allocation for each channel in the MIMO system by maximising the system's capacity [72]. This approach effectively 'shifts' the available transmitter power between LED sources so that the best channels use more power and, therefore, the maximum capacity achieved.

The water-filling algorithm allows different data streams to be transmitted at different power levels for each transmitter, with an overall transmitted power constraint. This requires complex control of the modulated power at each transmitter. The CCTC algorithm fixes the modulated power at each transmitter, and then 'steers' data to different patterns of transmitters to optimise data rate. This simplifies the system's design so that digital data is routed to different transmitter patterns, and fixed modulation circuitry can be used.

The fixed modulation power for each transmitter used in the CCTC algorithm will limit the system performance compared with the water-filling algorithm, which undertakes an overall

'optimum' search. The relative penalty is examined in section 3.5.5. This section presents a brief outline of the water-filling algorithm (see [73] for a full description).

The sum of the power of all LEDs P is set as a fixed value

$$\sum_{i=1}^{N_T} P_i = P \,, \tag{35}$$

where P_i is the modulation power of the ith LED.

The MIMO channel capacity is

$$C = \sum_{i=1}^{N_T} log_2(1 + \frac{P_i}{\sigma^2}\lambda_i) \,, \tag{36}$$

where σ^2 is the noise variance, and λ_i is the ith eigenvalue of the MIMO channel matrix.

To find the value of P_i maximising the capacity of the MIMO channel in (36) subject to (35), the Lagrangian function is introduced

$$\mathcal{L}(P_i, L) = \sum_{i=1}^{N_T} lg_2(1 + \frac{P_i\lambda_i}{\sigma^2}) + L(P - \sum_{i=1}^{N_T} P_i) \,, \tag{37}$$

where L is the Lagrange multiplier.

The solution of P_i can be found from the stationary point of $\mathcal{L}$, which is

$$P_i = (\mu - \frac{\sigma^2}{\lambda_i})^+ \,, \tag{38}$$

where μ is a constant and $(\alpha)^+ = \max(a, 0)$. Substituting (38) into (35), the value of μ can be obtained

$$\mu = \frac{P + \sum_{i=1}^{N_T} \frac{\sigma^2}{\lambda_i}}{N_T} . \tag{39}$$

3.5.4. Initial Up-Sampling Factor Prediction

As introduced in section 3.2, the neural network is only used to coordinate channels into one or several group(s). After the channel coordination, each channel group's data rate (up-sampling factor) is obtained using the CCTC algorithm. Each channel group has an initial up-sampling factor, which might be much greater or smaller than the optimal up-sampling factor. It takes time for the CCTC algorithm to obtain the optimal up-sampling factors.

In this section, the use of a neural network to determine the best up-sampling factors (and thus the best channel data rates) is investigated so that the neural network can replace the entire CCTC algorithm developed in Chapter II.

After the first neural network determines the optimal channel group(s), the second neural network predicts the up-sampling factor, further reducing computing time.

The problem is an input-output fitting problem, which means a mapping is required between a numeric input data set and a numeric output data set [74]. A two-layer neural network is applied here, including one input layer, one hidden layer and one output layer with linear neurons. The hidden layer neurons use the sigmoid function, and the output neurons are linear. The Bayesian regularisation algorithm is selected as the training algorithm.

The neural network input is the channel matrix after being processed by the transmitter coordination stage (mentioned in section 3.2). The transmitter coordination stage decides which columns in the matrix would form a ganging group, and these columns are added together. Zeros are added at the end of the matrix to ensure the number of neurons on the input side is a constant number $N_r \times N_t = 28$. The hidden layer possesses 10 neurons. The number of neurons at the output side is 4, representing the up-sampling factors of the corresponding channel groups separately. The last three values of the output neurons can be 0 when the system is partial or full ganging. The up-sampling factors at the output are rounded to integers and

used to estimate the initial up-sampling factors at the second stage of the simulation. After that, the function of the CCTC algorithm (line 4-28 in Algorithm 1 in section 2.5) is used to check if the predicted up-sampling factor achieves the optimal data rates and satisfies the BER requirement. The algorithm will make a minor adjustment on the values of the up-sampling factors to ensure it satisfies all the requirements.

3.5.5. Performance Evaluation

In this section, the performance of the MLP ANN-based system is evaluated. The mean aggregate data rates across the room obtained from the MLP ANN-based system are compared with the data rates of the system obtained with the CCTC algorithm, water-filling algorithm, pure ganging and SMP.

First, the simulation settings are given. The parameters applied in the system is shown in Table X. The total transmitted power is 4W. The system with the water-filling algorithm has flexible power for each LED while other systems have fixed power, 1 W, for each LED. The system model is the same as the model in section 2.1 with parameters in Table I.

Table X. Parameters

Parameters	**Values**
Number of movement periods in ORWP model (n)	341
Number of destinations in ORWP model (k)	30
Total power of four LEDs	4W

Training data applied in the system is shown in Table XI.

Table XI. Training data sets

Room size	**Azimuth angle (φ)**	**Polar angle (θ)**	**Array pitch**
7m × 7m × 3m	30°	0°	0.5m
	30°i with $i = 0,1,2$ with $i = 3,4,6,8,10$	30°	0.5m
			1m
7m × 7m × 2.5m	30°i with $i = 0,1,2$	30°	1m

Fig. 39 shows the mean aggregate data rate versus the receiver's distance to the room centre for the system with the MLP ANN, CCTC algorithm, water-filling algorithm, pure ganging and SMP.

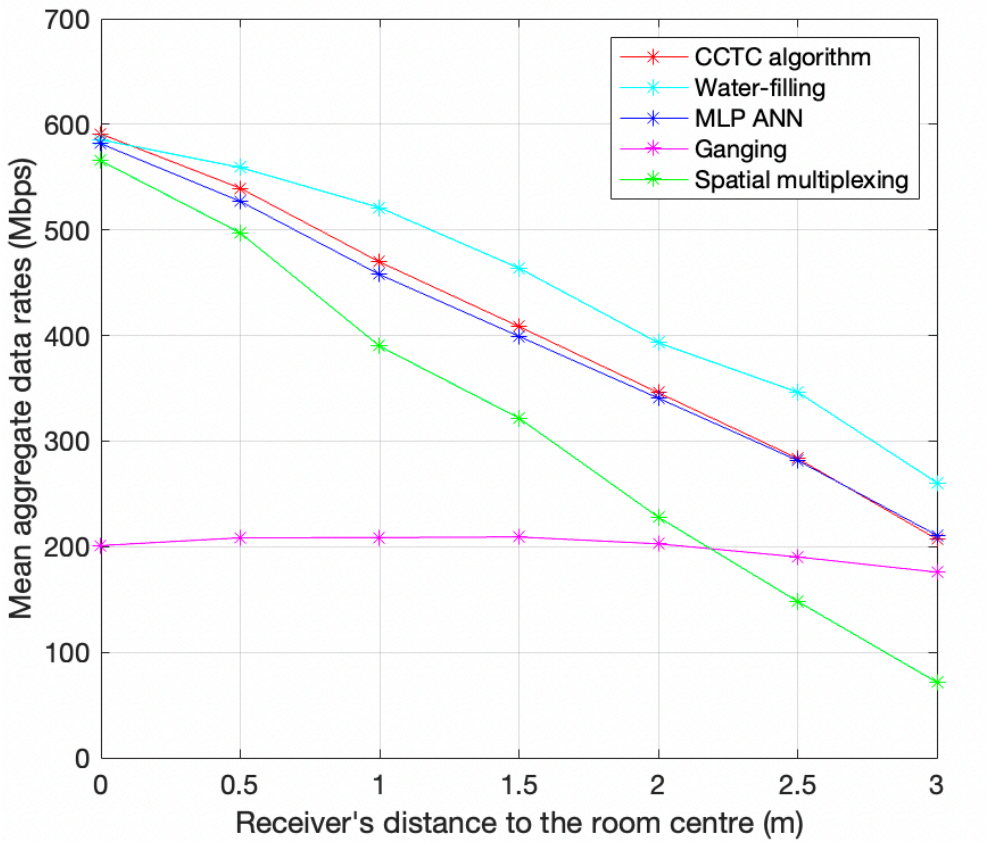
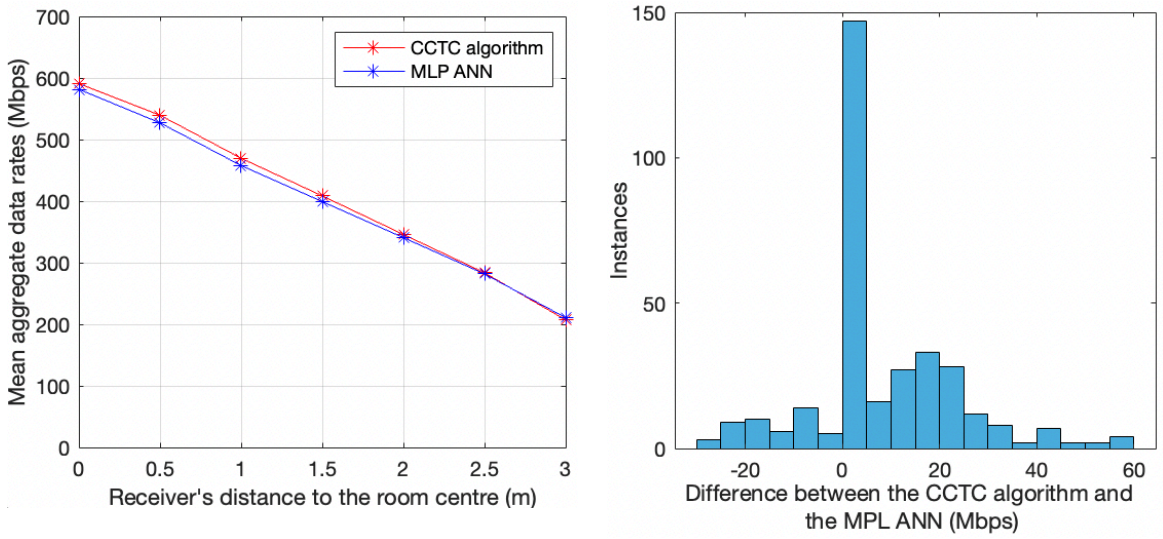


Figure 39. Mean aggregate data rates versus distance to the room centre.

First, the neural network's performance is examined by comparing the result with the CCTC algorithm. The plots obtained with the MLP ANN and CCTC algorithm are redrawn in Fig. 40 below to make the comparison clearer. Fig. 40(a) presents the mean aggregate data rates comparison for the MLP ANN and the CCTC algorithm, in which the MLP ANN shows comparable performance to the CCTC algorithm in obtaining the optimal transmitter pattern and the optimal mean aggregate data rates. Fig. 40(b) presents the difference histogram of the mean aggregate data rates between the two techniques. Most data are gathered around the zero-error line with a minor amount of data spread out within a limited range, showing good agreement between the two approaches. The neural network gives reliable performance across the room even with the mobile device user model and random device orientation.



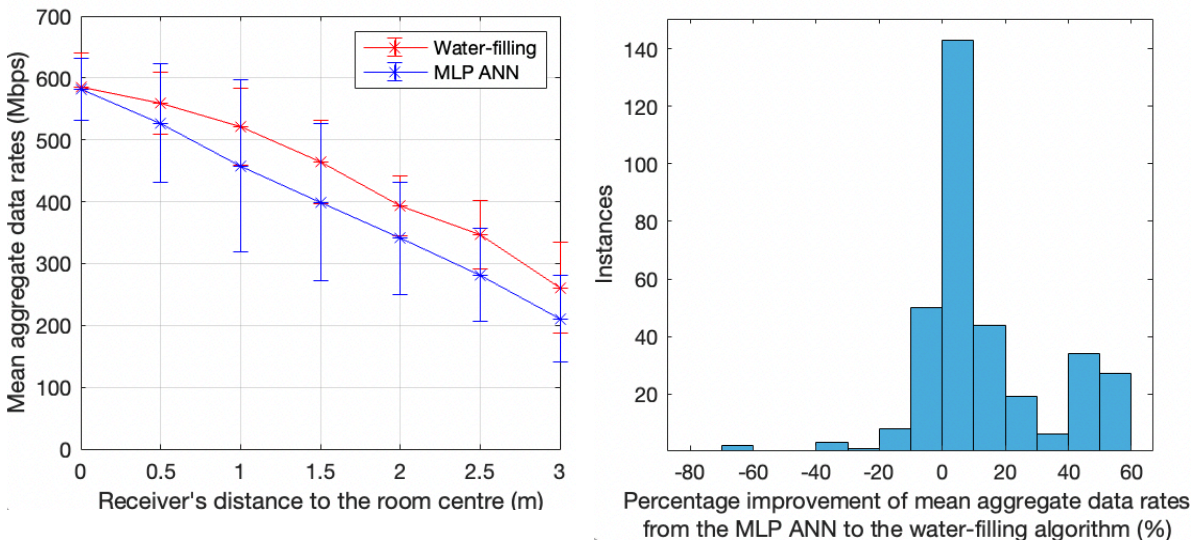
(a) (b)

Figure 40. (a) Mean aggregate data rates comparison for the CCTC algorithm and the MLP ANN, (b) Difference histogram for the CCTC algorithm and the MLP ANN.

Second, the lines representing the systems with the MLP ANN, ganging and SMP are analysed. Fig. 39 shows that the MLP ANN achieves a much higher mean aggregate data rate than pure ganging and SMP across the room. The reason is that the MLP ANN can switch among pure ganging, partial ganging and SMP according to the channel condition to optimise

the data rates. When the MIMO matrix is ill-conditioned near room corners, the MLP ANN uses a ganging scheme to group all the channels to transmit the same data, minimising the multi-stream interference between different channels. When the channel conditions improve from the room corner to the room centre, the system can adaptively switch to partial ganging or pure SMP to replace the full ganging approach and achieve a higher data rate.

Third, as mentioned before, the water-filling algorithm is employed as a benchmark to achieve the maximum capacity (and optimal data rate) of the system, revealing the trade-off between the reduced computational complexity and the decreased data rate. Fig. 41 gives a comparison between the MLP ANN and the water-filling algorithm. The performance is evaluated in two forms, as shown in Fig. 41(a) and Fig. 41(b). Fig. 41(a) shows the mean aggregate data rates for the system using the MLP ANN and the water-filling algorithm. The bars represent the spread of the values for a particular distance from the room centre and represent one standard deviation (one-sigma) from the mean value of the data rate for this distance. The water-filling algorithm gives higher mean aggregate data rates, especially when the receiver's distance to the room centre is larger than 1m. The MLP ANN also shows a larger variation in rates than the water-filling algorithm in the middle of the room.



(a) (b)

Figure 41. (a) Mean aggregate data rates for the water-filling algorithm and the MLP ANN with the difference bar, (b) Difference histogram for the water-filling algorithm and the MLP ANN.

Fig. 41(b) presents the normalised difference histogram of the mean aggregate data rates between the water-filling algorithm and the MLP ANN. The normalised difference is calculated as the measure of the percentage penalty of the MLP ANN approach compared with the water-filling algorithm. After the calculation, the MLP ANN has an average of 12 per cent lower capacity when compared with the water-filling algorithm.

Although the MLP ANN has a penalty on the data rate performance, it has advantages compared with the water-filling algorithm in several aspects:

(1) Computing time

Table XII shows a computing time comparison of the CCTC, water-filling and MLP ANN approaches. The computing time of the MLP ANN-based system is three times faster than that of the water-filling algorithm-based system. Both stages in the MLP ANN (the transmitter coordination stage and the up-sampling factor coordination stage) save

computing time. The water-filling algorithm-based system can only employ exhaustive search to do the up-sampling factor coordination, which spends more time than the neural network.

Table XII. Computing time comparison

Approach	**Computing time**	**Average data rate**
CCTC	1.278×10^5s = 35.49h	404.9Mbps
Water filling	1.089×10^5s = 30.24h	448.99Mbps
Neural network	3.528×10^4 s = 9.78h	397.35Mbps

(2) Lighting sources

The MLP ANN-based system moves data around the fixtures, which only needs fixed drive current devices. The water-filling algorithm has flexible power levels, which means a more complex controller for the source is required.

(3) Illumination

The MLP ANN-based system offers stable illumination. The water-filling algorithm concentrates all the power to one or two LEDs when required. The unbalanced power distribution among LEDs may cause the dimming and colour inconsistency problem [75].

In summary, there is a trade-off between the MLP ANN and the water-filling approach. The MLP ANN is demonstrated as a fast and simple alternative to replace the complex water-filling algorithm in the MIMO-VLC system. Moreover, the MLP ANN has the potential to find the optimal transmitter pattern with only the receiver position data as the input in the future. The conclusions and the future work will be presented and discussed in the next chapter.

CHAPTER IV: CONCLUSIONS AND FUTURE WORK

4.1. Conclusions

This thesis aims to demonstrate a high-speed MIMO-VLC system with data rate-adaptive modulation and transmitter pattern coordination without and with the neural network.

Chapter I presents the principles of VLC and a literature review of VLC systems, MIMO-VLC systems, channel compensation techniques, and relevant challenges. VLC with its broad unlicensed spectrum is investigated to alleviate the wireless communications spectrum 'drought'. MIMO-VLC with multiple transmitters and multiple receivers is developed from conventional VLC, enabling higher spectral efficiency and high-speed data communication. The employment of MIMO brings multi-stream interference when a receiver detects signals from multiple transmitters. Spatial diversity, spatial multiplexing, and spatial modulation are introduced to mitigate the interference. Apart from the multi-stream interference, other critical challenges for MIMO-VLC include inter-symbol interference (ISI) and selection of proper receiver design. The solutions are explored in the following chapters.

Chapter II reports a high-speed VLC system with data rate-adaptive modulation and a new Channel Condition-based Transmitter Coordination (CCTC) algorithm. In the algorithm, the MIMO channels are grouped into one or several ganging groups, and each ganging group's data rate (up-sampling factor) is separately optimised. The system also employs zero-forcing MIMO equalisation and a decision feedback equaliser (DFE) to mitigate multi-stream interference and inter-symbol interference. MIMO systems require multi-channel receivers, and two types of angular diversity receivers with similar sizes are compared: A seven-channel angle diversity receiver (ADR) and an aperture-based receiver (ABR). The ADR achieves angular diversity by differentiating the orientation among receiver elements (REs), and the

ABR achieves angular diversity by differentiating relative positions between apertures and REs. The proposed channel adaptive system outperforms the conventional spatial multiplexing system by 41 per cent for the seven-channel ADR and 127 per cent for the ABR on average. In the proposed system, the peak overall data rate of the seven-channel ADR (676 Mbps) is higher than that of the ABR (434 Mbps) by 56 per cent. The average overall data rate for the seven-channel ADR is 64 per cent higher than that of the ABR. Results show that the ADR performs better than the ABR due to its larger usable detection area and smaller influence of the ambient noise. Hence, the ADR is used in subsequent investigations.

Work in Chapter II shows that data rate-adaptive modulation and the CCTC algorithm provide much better performance compared with the conventional MIMO scheme, as grouping poor channels together provides better overall performance than transmitting individual data streams over the same channels. However, the computational complexity is still high for the CCTC algorithm, and an approach that reduces this is discussed in Chapter III.

Chapter III explores the solution to decrease the high computing complexity of the CCTC algorithm in Chapter II. There are two stages in the CCTC algorithm: The optimal transmitter pattern is coordinated in the first stage, and the optimal up-sampling factor of each transmitter group is determined in the second. Feedforward multi-layer perceptron (MLP) artificial neural networks (ANNs) are employed to replace both stages in the CCTC algorithm to predict the optimal transmitter pattern and save computing time.

A series of tests are undertaken for different receiver positions and orientations (yaw and roll rotation). In each case, the set of positions and orientations used by the training data is limited. The MLP ANN performs well during the test by obtaining the optimal transmitter pattern and saves more than a factor of three in computing time compared with the CCTC algorithm while obtaining the same system performance. Further, the MLP ANN is robust and can predict the optimal pattern for receiver positions in rooms with different geometries and

are not limited to the scope of the training data. Afterwards, a final series of tests are undertaken using a statistical model for the position and orientation of a receiver on a mobile device to simulate a real-life user walking within a room. A good performance is obtained.

In order to test the overall performance of the MLP ANN, a water-filling approach is used as a comparison. In this system, each LED is allocated a variable level of power and optimally equalised, so that the optimal overall data rate is obtained. The water-filling algorithm is complex in its control and implementation, but it provides a valuable benchmark. Data show that the MLP ANN has an average of 12 per cent reduction in the mean aggregate data rates than the water-filling algorithm. However, the MLP ANN saves more than three times in computing time than the water-filling algorithm, indicating the superior utility of the MLP ANN approach.

In conclusion: First, the employment of data rate-adaptive modulation and the CCTC algorithm achieves a higher speed VLC than the conventional MIMO scheme. Second, the MLP ANNs have been introduced to accelerate the pattern coordination and up-sampling factor coordination in the CCTC algorithm, which significantly decreases the computational complexity while achieving the same data rate performance as the CCTC algorithm. After this, the MLP ANN-based system is compared with the water-filling algorithm. With a factor of three improvements on computing time of the MLP ANN compared with the water-filling algorithm, the reduction on the aggregate data rates of the MLP ANN is acceptable. The adaptive MIMO-VLC is shown to be an efficient and easy technique that can be further studied.

4.2. Future Plan

This chapter suggests several potential approaches for further improvements of the proposed system.

4.2.1. Advanced Neural Network-Based Transmitter Pattern Coordination

- **Employ Neural Network with the Water-Filling Algorithm**

Currently, the water-filling algorithm-based system costs three times of computing time compared with the neural network-based system. One of the reasons is that the neural network-based system uses two neural networks to predict: (1) the optimal transmitter pattern, and (2) the optimal up-sampling factors separately, which saves a large amount of computing time. In the water-filling algorithm-based system, only spatial multiplexing is used but with variable power allocation based on the channel conditions. Hence, the transmitter pattern coordination at stage (1) is not needed. However, a neural network can still be applied to approximately predict the optimal up-sampling factors at stage (2) for the water-filling algorithm-based system to reduce the computational complexity.

- **Employ Receiver Position Information as the Input**

The neural network explored in Chapter IV can predict the optimal transmitter pattern and up-sampling factors with the channel matrix as the input. However, the channel state information constantly changes and cannot be obtained immediately for a mobile receiver. Hence, the neural network requires an input that is easier to be captured from the mobile user.

The MIMO channel matrix can be calculated from (4) and (5) in section 2.1.2. The values in the MIMO channel matrix are based on: (1) the collection area of the receiver element (RE), (2) the distance between each RE and LED, (3) the irradiance angle at LED to RE, and (4) the incident angle at RE to LED. The collection area of the RE is expected to be a fixed value for a receiver. Other variables are all related to the relative position and orientation between the LED and the RE. Hence, there is enormous potential to directly employ the position and orientation of the LEDs and the REs as input data to derive the optimal transmitter pattern. The receiver position information is more straightforward to be captured than the channel state information, as shown in [63], [64], so there may be significant benefits in terms of complexity.

4.2.2. Hybrid Indoor OWC with Beam-Steering

- **Incorporate Beam-steering into the Existing System**

In the proposed system in section 2.6.2, the highest overall data rate is approximately 676 Mbps near the room centre for the seven-channel ADR. However, the lowest overall data rate is approximately 160 Mbps near the room corners, much lower than the peak overall data rate. Incorporating beam-steering into the existing well-established model can provide a higher data rate to the user, especially near the room corners. It can also improve the current system's coverage, reliability and capacity [76]. Beam-steering is one of the interests of the author's group. The hardware prototype with fully automate tracking has been implemented in the Oxford laboratory [77], [78]. Therefore, the cooperation of the beam-steering sources and the existing wide and non-steerable LED sources is a fruitful area of future work.

REFERENCES

[1] G. Staple and K. Werbach, 'The end of spectrum scarcity', *IEEE Spectr.*, vol. 41, no. 3, pp. 48–52, Mar. 2004, doi: 10.1109/MSPEC.2004.1270548.

[2] A. Mansour, R. Mesleh, and M. Abaza, 'New challenges in wireless and free space optical communications', *Optics and Lasers in Engineering*, vol. 89, pp. 95–108, May 2016, doi: 10.1016/j.optlaseng.2016.03.027.

[3] P. H. Pathak, X. Feng, P. Hu, and P. Mohapatra, 'Visible light communication, networking, and sensing: A survey, potential and challenges', *IEEE Commun. Surv. Tutorials*, vol. 17, no. 4, pp. 2047–2077, 2015, doi: 10.1109/COMST.2015.2476474.

[4] F. E. Goodwin, 'A Review of Operational Laser Communication Systems', *Proceedings of the IEEE*, vol. 58, no. 10, pp. 1746–1752, 1970, doi: 10.1109/PROC.1970.7998.

[5] A. Jovicic, J. Li, and T. Richardson, 'Visible light communication: Opportunities, challenges and the path to market', *IEEE Commun. Mag.*, vol. 51, no. 12, pp. 26–32, Dec. 2013, doi: 10.1109/MCOM.2013.6685754.

[6] L. Zeng *et al.*, 'High data rate multiple input multiple output (MIMO) optical wireless communications using white led lighting', *IEEE J. Select. Areas Commun.*, vol. 27, no. 9, pp. 1654–1662, Dec. 2009, doi: 10.1109/JSAC.2009.091215.

[7] L. Grobe *et al.*, 'High-speed visible light communication systems', *IEEE Commun. Mag.*, vol. 51, no. 12, pp. 60–66, Dec. 2013, doi: 10.1109/MCOM.2013.6685758.

[8] M. A. Khalighi and M. Uysal, 'Survey on free space optical communication: A communication theory perspective', *IEEE Communications Surveys and Tutorials*, vol. 16, no. 4, pp. 2231–2258, 2014, doi: 10.1109/COMST.2014.2329501.

[9] F. Zafar, M. Bakaul, and R. Parthiban, 'Laser-Diode-Based Visible Light Communication: Toward Gigabit Class Communication', *IEEE Commun. Mag.*, vol. 55, no. 2, pp. 144–151, Feb. 2017, doi: 10.1109/MCOM.2017.1500672CM.

[10] Y. Narukawa, M. Ichikawa, D. Sanga, M. Sano, and T. Mukai, 'White light emitting diodes with super-high luminous efficacy', *J. Phys. D: Appl. Phys.*, vol. 43, no. 35, p. 354002, Sep. 2010, doi: 10.1088/0022-3727/43/35/354002.

[11] P. A. Haigh, Z. Ghassemlooy, S. Rajbhandari, I. Papakonstantinou, and W. Popoola, 'Visible Light Communications: 170 Mb/s Using an Artificial Neural Network Equalizer in a Low Bandwidth White Light Configuration', *J. Lightwave Technol.*, vol. 32, no. 9, pp. 1807–1813, May 2014, doi: 10.1109/JLT.2014.2314635.

[12] H. Le Minh *et al.*, 'High-speed visible light communications using multiple-resonant equalization', *IEEE Photon. Technol. Lett.*, vol. 20, no. 14, pp. 1243–1245, Jul. 2008, doi: 10.1109/LPT.2008.926030.

[13] H. Ma, L. Lampe, and S. Hranilovic, 'Coordinated Broadcasting for Multiuser Indoor Visible Light Communication Systems', *IEEE Trans. Commun.*, vol. 63, no. 9, pp. 3313–3324, Sep. 2015, doi: 10.1109/TCOMM.2015.2452254.

[14] M. Rahaim and T. D. C. Little, 'SINR analysis and cell zooming with constant illumination for indoor VLC networks', in *2013 2nd International Workshop on Optical Wireless Communications (IWOW)*, Newcastle upon Tyne, United Kingdom, Oct. 2013, pp. 20–24. doi: 10.1109/IWOW.2013.6777769.

[15] S. Collins, D. C. O'Brien, and A. Watt, 'High gain, wide field of view concentrator for optical communications', *Opt. Lett.*, vol. 39, no. 7, pp. 1756–1759, Apr. 2014, doi: 10.1364/OL.39.001756.

[16] Y. Tanaka, S. Haruyama, and M. Nakagawa, 'Wireless optical trasnsmissions with white colored LED for wireless home links', *IEEE International Symposium on Personal, Indoor and Mobile Radio Communications, PIMRC*, vol. 2, pp. 1325–1329, 2000, doi: 10.1109/pimrc.2000.881634.

[17] Y. Tanaka, T. Komine, S. Haruyama, and M. Nakagawa, 'Indoor visible communication utilizing plural white LEDs as lighting', *IEEE International Symposium on Personal, Indoor and Mobile Radio Communications, PIMRC*, vol. 2, 2001, doi: 10.1109/pimrc.2001.965300.

[18] T. Komine and M. Nakagawa, 'Fundamental analysis for visible-light communication system using LED lights', *IEEE Transactions on Consumer Electronics*, vol. 50, no. 1, pp. 100–107, 2004, doi: 10.1109/TCE.2004.1277847.

[19] M. Y. Abualhoul, M. Marouf, O. Shagdar, and F. Nashashibi, 'Platooning control using visible light communications: A feasibility study', in *16th International IEEE Conference on Intelligent Transportation Systems (ITSC 2013)*, The Hague, Netherlands, Oct. 2013, pp. 1535–1540. doi: 10.1109/ITSC.2013.6728448.

[20] S. Rajagopal, R. Roberts, and S.-K. Lim, 'IEEE 802.15.7 visible light communication: modulation schemes and dimming support', *IEEE Commun. Mag.*, vol. 50, no. 3, pp. 72–82, Mar. 2012, doi: 10.1109/MCOM.2012.6163585.

[21] D. O'Brien, S. Rajbhandari, and H. Chun, 'Transmitter and receiver technologies for optical wireless', *Phil. Trans. R. Soc. A.*, vol. 378, no. 2169, p. 20190182, Apr. 2020, doi: 10.1098/rsta.2019.0182.

[22] S. Al-Ahmadi, O. Maraqa, M. Uysal, and S. M. Sait, 'Multi-User Visible Light Communications: State-of-the-Art and Future Directions', *IEEE Access*, vol. 6, pp. 70555–70571, 2018, doi: 10.1109/ACCESS.2018.2879885.

[23] K. D. Dambul, D. C. O'Brien, and G. Faulkner, 'Indoor optical wireless MIMO system with an imaging receiver', *IEEE Photonics Technology Letters*, vol. 23, no. 2, pp. 97–99, 2011, doi: 10.1109/LPT.2010.2091627.

[24] T. Fath and H. Haas, ‘Performance comparison of MIMO techniques for optical wireless communications in indoor environments’, *IEEE Transactions on Communications*, vol. 61, no. 2, pp. 733–742, 2013, doi: 10.1109/TCOMM.2012.120512.110578.

[25] C. Chen, W. De Zhong, H. Yang, and P. Du, ‘On the Performance of MIMO-NOMA-Based Visible Light Communication Systems’, *IEEE Photonics Technology Letters*, vol. 30, no. 4, pp. 307–310, 2018, doi: 10.1109/LPT.2017.2785964.

[26] D. Gesbert, M. Shafi, D. S. Shiu, P. J. Smith, and A. Naguib, ‘From theory to practice: An overview of MIMO space-time coded wireless systems’, *IEEE Journal on Selected Areas in Communications*, vol. 21, no. 3, pp. 281–302, 2003, doi: 10.1109/JSAC.2003.809458.

[27] J. Lian and M. Brandt-Pearce, ‘Multiuser MIMO Indoor Visible Light Communication System Using Spatial Multiplexing’, *J. Lightwave Technol.*, vol. 35, no. 23, pp. 5024–5033, Dec. 2017, doi: 10.1109/JLT.2017.2765462.

[28] C. He, T. Q. Wang, and J. Armstrong, ‘Performance comparison between spatial multiplexing and spatial modulation in indoor MIMO visible light communication systems’, presented at the 2016 IEEE International Conference on Communications (ICC), Kuala Lumpur, Malaysia, May 2016. doi: 10.1109/ICC.2016.7511379.

[29] P. M. Butala, H. Elgala, and T. D. C. Little, ‘Performance of optical spatial modulation and spatial multiplexing with imaging receiver’, in *2014 IEEE Wireless Communications and Networking Conference (WCNC)*, Istanbul, Turkey, Apr. 2014, pp. 394–399. doi: 10.1109/WCNC.2014.6952040.

[30] R. Mesleh, H. Haas, C. W. Ahn, and S. Yun, ‘Spatial Modulation - A New Low Complexity Spectral Efficiency Enhancing Technique’, presented at the 2006 First International Conference on Communications and Networking in China, Beijing, China, Oct. 2006. doi: 10.1109/CHINACOM.2006.344658.

[31] R. Mesleh, H. Elgala, and H. Haas, 'Optical spatial modulation', *Journal of Optical Communications and Networking*, vol. 3, no. 3, pp. 234–244, 2011, doi: 10.1364/JOCN.3.000234.

[32] E. Poves, W. Popoola, H. Haas, J. Thompson, and D. Cárdenas, 'Experimental Results on the Performance of Optical Spatial Modulation Systems', in *2012 IEEE Vehicular Technology Conference (VTC Fall)*, Quebec City, QC, Canada, Sep. 2012, pp. 1–5. doi: 10.1109/VTCFall.2012.6399111.

[33] N. Ishikawa and S. Sugiura, 'Maximizing constrained capacity of power-imbalanced optical wireless MIMO communications using spatial modulation', *Journal of Lightwave Technology*, vol. 33, no. 2, pp. 519–527, 2015, doi: 10.1109/JLT.2015.2391198.

[34] W. Popoola, E. Poves, and H. Haas, 'Generalised space shift keying for visible light communications', presented at the 2012 8th International Symposium on Communication Systems, Networks & Digital Signal Processing (CSNDSP 2012), Poznan, Poland, Jul. 2012. doi: 10.1109/CSNDSP.2012.6292784.

[35] R. Mulyawan *et al.*, 'MIMO visible light communications using a wide field-of-view fluorescent concentrator', *IEEE Photonics Technology Letters*, vol. 29, no. 3, pp. 306–309, 2017, doi: 10.1109/LPT.2016.2647717.

[36] K.-H. Park, Y.-C. Ko, and M.-S. Alouini, 'A novel power and offset allocation method for spatial multiplexing MIMO Systems in optical wireless channels', in *2011 IEEE GLOBECOM Workshops (GC Wkshps)*, Houston, TX, USA, Dec. 2011, pp. 823–827. doi: 10.1109/GLOCOMW.2011.6162569.

[37] B. Li, J. Wang, R. Zhang, H. Shen, C. Zhao, and L. Hanzo, 'Multiuser MISO transceiver design for indoor downlink visible light communication under per-LED optical power constraints', *IEEE Photonics Journal*, vol. 7, no. 4, pp. 1–15, 2015, doi: 10.1109/JPHOT.2015.2446203.

[38] H. Sifaou, K.-H. Park, A. Kammoun, and M.-S. Alouini, 'Optimal linear precoding for indoor visible light communication system', in *2017 IEEE International Conference on Communications (ICC)*, Paris, France, May 2017, pp. 1–5. doi: 10.1109/ICC.2017.7997330.

[39] F. E. Alsaadi and J. M. H. Elmirghani, 'Mobile Multi-Gigabit Spot-Diffusing Optical Wireless System Employing Beam Angle and Power Adaptation and Imaging Reception', in *2010 IEEE Global Telecommunications Conference GLOBECOM 2010*, Miami, FL, USA, Dec. 2010, pp. 1–6. doi: 10.1109/GLOCOM.2010.5683931.

[40] T. Q. Wang, C. He, and J. Armstrong, 'Angular diversity for indoor MIMO optical wireless communications', in *2015 IEEE International Conference on Communications (ICC)*, London, Jun. 2015, pp. 5066–5071. doi: 10.1109/ICC.2015.7249127.

[41] J. M. Kahn and J. R. Barry, 'Wireless infrared communications', *Proceedings of the IEEE*, vol. 85, no. 2, pp. 265–298, Feb. 1997, doi: 10.1109/5.554222.

[42] A. Nuwanpriya, S. W. Ho, and C. S. Chen, 'Indoor MIMO Visible Light Communications: Novel Angle Diversity Receivers for Mobile Users', *IEEE Journal on Selected Areas in Communications*, vol. 33, no. 9, pp. 1780–1792, 2015, doi: 10.1109/JSAC.2015.2432514.

[43] J. B. Carruthers and J. M. Kahn, 'Angle diversity for nondirected wireless infrared communication', *IEEE Trans. Commun.*, vol. 48, no. 6, pp. 960–969, Jun. 2000, doi: 10.1109/26.848557.

[44] T. Q. Wang, C. He, and J. Armstrong, 'Performance analysis of aperture-based receivers for MIMO IM/DD visible light communications', *Journal of Lightwave Technology*, vol. 35, no. 9, pp. 1513–1523, 2017, doi: 10.1109/JLT.2016.2641002.

[45] L. U. Khan, 'Visible light communication: Applications, architecture, standardization and research challenges', *Digital Communications and Networks*, vol. 3, no. 2, pp. 78–88, 2017, doi: 10.1016/j.dcan.2016.07.004.

[46] L. E. M. Matheus, A. B. Vieira, L. F. M. Vieira, M. A. M. Vieira, and O. Gnawali, 'Visible Light Communication: Concepts, Applications and Challenges', *IEEE Communications Surveys and Tutorials*, vol. 21, no. 4, pp. 3204–3237, 2019, doi: 10.1109/COMST.2019.2913348.

[47] A. J. C. Moreira, R. T. Valadas, and A. M. De Oliveira Duarte, 'Optical interference produced by artificial light', *Wireless Networks*, vol. 3, no. 2, pp. 131–140, 1997, doi: 10.1023/A:1019140814049.

[48] L. Zeng, D. O'Brien, H. Le-Minh, K. Lee, D. Jung, and Y. Oh, 'Improvement of Data Rate by using Equalization in an Indoor Visible Light Communication System', in *2008 4th IEEE International Conference on Circuits and Systems for Communications*, Shanghai, China, May 2008, pp. 678–682. doi: 10.1109/ICCSC.2008.149.

[49] D. C. O'Brien and M. Katz, 'Optical wireless communications within fourth-generation wireless systems [Invited]', *Journal of Optical Networking*, vol. 4, no. 6, pp. 312–322, 2005, doi: 10.1364/JON.4.000312.

[50] J. C. A. Barata and M. S. Hussein, 'The Moore-Penrose Pseudoinverse: A Tutorial Review of the Theory', *Brazilian Journal of Physics*, vol. 42, no. 1–2, pp. 146–165, 2012, doi: 10.1007/s13538-011-0052-z.

[51] J. M. Cioffi, G. P. Dudevoir, M. V. Eyuboglu, and G. D. Forney, 'MMSE Decision-Feedback Equalizers and Coding—Part I: Equalization Results', *IEEE Transactions on Communications*, vol. 43, no. 10, pp. 2582–2594, 1995, doi: 10.1109/26.469441.

[52] J.-P. Javaudin, M. Bellec, D. Varoutas, and V. Suraci, 'OMEGA ICT project: Towards Convergent Gigabit Home Networks', presented at the IEEE International Symposium on Personal, Indoor and Mobile Radio Communications (IEEE PIMRC), Sep. 2008. doi: 10.1109/PIMRC.2008.4699838.

[53] E. F. Schubert, ‘White-light sources based on LEDs’, in *Light-Emitting Diodes*, 2nd ed., Cambridge, U.K.: Cambridge University Press, 2006, pp. 332–345. doi: 10.1017/CBO9780511790546.

[54] S. K.R., ‘Effects of electro-thermal conditions on luminous efficacies of phosphor-converted white light emitting diodes’, in *2018 International Conference on Computational Techniques, Electronics and Mechanical Systems (CTEMS)*, Belgaum, India, Dec. 2018, pp. 51–55. doi: 10.1109/CTEMS.2018.8769139.

[55] C. Jenila and R. K. Jeyachitra, ‘Performance analysis of indoor joint illumination and communication systems using light emitting diodes and laser diodes’, in *2017 International Conference on Wireless Communications, Signal Processing and Networking (WiSPNET)*, Chennai, Mar. 2017, pp. 905–910. doi: 10.1109/WiSPNET.2017.8299893.

[56] J. G. Proakis and M. Salehi, *Digital Communications*, 5th ed. Boston, USA: McGraw-Hill, 2008.

[57] T. Komine, J. H. Lee, S. Haruyama, and M. Nakagawa, ‘Adaptive equalization system for visible light wireless communication utilizing multiple white led lighting equipment’, *IEEE Transactions on Wireless Communications*, vol. 8, no. 6, pp. 2892–2900, 2009, doi: 10.1109/TWC.2009.060258.

[58] T. S. Rappaport, *Wireless Communications: Principles and Practice*. New York, NY, USA: Prentic Hall PTR, 1996.

[59] R. H. Kwong and E. W. Johnston, ‘A variable step size LMS algorithm’, *IEEE Trans. Signal Process.*, vol. 40, no. 7, pp. 1633–1642, Jul. 1992, doi: 10.1109/78.143435.

[60] *Forward error correction for high bit-rate DWDM submarine systems*, ITU-T G.975.1, International Telecommunication Union, 2004.

[61] S. Bhama and H. Singh, ‘Single layer neural networks for linear system identification using gradient descent technique’, *IEEE Trans. Neural Netw.*, vol. 4, no. 5, pp. 884–888, Sep. 1993, doi: 10.1109/72.248467.

[62] S. Agatonovic-Kustrin and R. Beresford, ‘Basic concepts of artificial neural network (ANN) modeling and its application in pharmaceutical research’, *Journal of Pharmaceutical and Biomedical Analysis*, vol. 22, no. 5, pp. 717–727, 2000, doi: 10.1016/S0731-7085(99)00272-1.

[63] W. Sayed, T. Ismail, and K. Elsayed, ‘A Neural Network-Based VLC Indoor Positioning System for Moving Users’, presented at the 2019 International Conference on Smart Applications, Communications and Networking (SmartNets), Sharm El Sheik, Egypt, Dec. 2019. doi: 10.1109/SmartNets48225.2019.9069785.

[64] J. He *et al.*, ‘Demonstration of high precision 3D indoor positioning system based on two-layer ANN machine learning technique’, in *Optical Fiber Communication Conference (OFC) 2019*, San Diego, California, 2019, p. Th3I.2. doi: 10.1364/OFC.2019.Th3I.2.

[65] S. A. I. Alfarozi, K. Pasupa, H. Hashizume, K. Woraratpanya, and M. Sugimoto, ‘Robust and Unified VLC Decoding System for Square Wave Quadrature Amplitude Modulation Using Deep Learning Approach’, *IEEE Access*, vol. 7, pp. 163262–163276, 2019, doi: 10.1109/ACCESS.2019.2952465.

[66] S. Ma *et al.*, ‘Signal Demodulation with Machine Learning Methods for Physical Layer Visible Light Communications: Prototype Platform, Open Dataset, and Algorithms’, *IEEE Access*, vol. 7, pp. 30588–30598, 2019, doi: 10.1109/ACCESS.2019.2903375.

[67] D.-D. Le, D.-P. Nguyen, T.-H. Tran, and Y. Nakashima, ‘Run-Length Limited Decoding for Visible Light Communications: A Deep Learning Approach’, in *2019 25th Asia-Pacific Conference on Communications (APCC)*, Ho Chi Minh City, Vietnam, Nov. 2019, pp. 496–501. doi: 10.1109/APCC47188.2019.9026486.

[68] S. Rajbhandari *et al.*, 'Neural Network-Based Joint Spatial and Temporal Equalization for MIMO-VLC System', *IEEE Photonics Technology Letters*, vol. 31, no. 11, pp. 821–824, 2019, doi: 10.1109/LPT.2019.2909139.

[69] M. D. Soltani, A. A. Purwita, Z. Zeng, H. Haas, and M. Safari, 'Modeling the Random Orientation of Mobile Devices: Measurement, Analysis and LiFi Use Case', *IEEE Trans. Commun.*, vol. 67, no. 3, pp. 2157–2172, Mar. 2019, doi: 10.1109/TCOMM.2018.2882213.

[70] C. Bettstetter, H. Hartenstein, and X. Costa-Pérez, 'Stochastic Properties of the Random Waypoint Mobility Model', *Wireless Networks*, vol. 10, pp. 555–567, 2004, doi: 10.1145/570760.570761.

[71] A. A. Purwita, M. D. Soltani, M. Safari, and H. Haas, 'Terminal Orientation in OFDM-Based LiFi Systems', *IEEE Trans. Wireless Commun.*, vol. 18, no. 8, pp. 4003–4016, Sep. 2019, doi: 10.1109/TWC.2019.2920132.

[72] P. M. Butala, H. Elgala, and T. D. C. Little, 'SVD-VLC: A novel capacity maximizing VLC MIMO system architecture under illumination constraints', in *2013 IEEE Globecom Workshops (GC Wkshps)*, Dec. 2013, pp. 1087–1092. doi: 10.1109/GLOCOMW.2013.6825137.

[73] J. M. Cioffi. (2014). Advanced Digital Communications: Chapter 4 - Multi-channel Modulation. [Online]. Available: https://web.stanford.edu/class/ee379c/readerfiles/chap4.pdf

[74] M. Chen, U. Challita, W. Saad, C. Yin, and M. Debbah, 'Artificial Neural Networks-Based Machine Learning for Wireless Networks: A Tutorial', *IEEE Commun. Surv. Tutorials*, vol. 21, no. 4, pp. 3039–3071, 2019, doi: 10.1109/COMST.2019.2926625.

[75] A. T. L. Lee, H. Chen, and S.-C. Tan, ‘Precise Dimming and Color Control of LED Systems Based on Color Mixing’, *IEEE Transactions on Power Electronics*, vol. 31, no. 1, pp. 65–80, Jan. 2016, doi: 10.1109/TPEL.2015.2448641.

[76] M. B. Rahaim, J. Morrison, and T. D. C. Little, ‘Beam control for indoor FSO and dynamic dual-use VLC lighting systems’, *Journal of Communications and Information Networks*, vol. 2, no. 4, pp. 11–27, 2017, doi: 10.1007/s41650-017-0041-7.

[77] R. Singh *et al.*, ‘Design and Characterisation of Terabit/s Capable Compact Localisation and Beam-Steering Terminals for Fiber-Wireless-Fiber Links’, *Journal of Lightwave Technology*, vol. 38, no. 24, pp. 6817–6826, Dec. 2020, doi: 10.1109/JLT.2020.3022754.

[78] Y. Hong *et al.*, ‘Beyond Terabit/s WDM Optical Wireless Transmission using Wavelength-transparent Beam Tracking and Steering’, presented at the Optical Fiber Communication Conference, San Diego, CA, USA, May 2020. doi: 10.1364/OFC.2020.W1G.4.